

New Supersonic Wing Far-Field Composite-Element Wave-Drag Optimization Method

Brenda Kulfan*

The Boeing Company, Seattle, Washington 98124

DOI: 10.2514/1.42823

NASA and industry recently ended the High Speed Civil Transport program. The objective of the High Speed Civil Transport program was to develop critical technologies to support the potential development of viable supersonic commercial transport aircraft. The aerodynamic design development activities benefited greatly from the use of the prior design, analysis, and prediction methods as well as the understanding of the fundamental physics inherent in an efficient supersonic aircraft design. It was recognized that the critical strengths of the aerodynamic processes included the blending of the computational power offered by computational fluid dynamics methods with the fundamental knowledge and rapid design development and assessment capabilities inherent in the existing linear aerodynamic theory methods. Nonlinear design optimization studies are typically initiated with an initial optimized linear theory baseline configuration design. In this paper, a new supersonic linear theory wave-drag optimization methodology using far-field wave-drag methodology is introduced. The method is developed using the class-function/shape-function transformation concept of an analytic scalar wing definition. The methodology is applied to an arrow-wing planform to illustrate its versatility as well as to demonstrate the usefulness of the class-function/shape-function transformation analytic wing concept for aerodynamic design optimization.

I. Introduction

NASA and industry recently ended the High Speed Civil Transport (HSCT) program. The objective of the HSCT program was to develop critical technologies to support the potential development of viable supersonic commercial transport aircraft. The initial phases of the HSCT program used the extensive database of methods and knowledge and expertise from the U.S. Supersonic Transport (SST) program and the subsequent NASA-sponsored Supersonic Cruise Research studies. The aerodynamic design development activities benefited greatly from the use of the prior design, analysis, and prediction methods as well as the understanding of the fundamental physics inherent in an efficient supersonic aircraft design. The emerging advanced computational fluid dynamics (CFD) methods greatly enhanced the supersonic design and analysis process and enabled substantial improvements in achievable aerodynamic performance levels. It was recognized that the critical strengths of the aerodynamic processes included the blending of the computational power offered by CFD methods with the fundamental knowledge and rapid design development and assessment capabilities inherent in the existing linear aerodynamic theory methods. The primary objectives of this paper are twofold. First, the far-field composite-element (FCE) supersonic wave-drag optimization method will be developed and introduced. Second, the use of the universal parametric geometry representation method, the class-function/shape-function transformation technique (CST) [1–3], for wing design optimization will be demonstrated.

II. Planar Linear Theory Analyses Versus CFD Analyses

“Linear theory is long on ideas but short on arithmetic, CFD is long on arithmetic but short on ideas.”[†] Although linear theory can provide

some unique insights and ideas, it does require understanding of both the numerical and physical limitations of the theory. However, CFD can provide both answers and visibility for flow solutions and flow conditions far beyond the capability of linear theory. By using both CFD and linear theory and exploiting the benefits of each, we can have the ideas and the arithmetic with the added bonus of increased synergistic understanding and design capability.

Since the advent of the use of the powerful CFD design and analysis methods, the value of linear theory methods is often questioned. During the development cycle of a new airplane concept, an important question to be answered is how much detail and computational sophistication is required. The answer offered to this question in [4] is, “In the spirit of Prandtl, Taylor and von Kármán, the conscientious engineer will strive to use as conceptually simple an approach as possible to achieve his ends.”

Being old or restrictive does not imply being useless. In fact, many of the contributions derived from linear theory are still useful today: 1) elliptic load distribution for minimum induced drag; 2) thin-airfoil theory; 3) conformal transformations; 4) supersonic area-rule wave-drag calculation; 5) transfer-rule wing/body optimization; 6) Sears–Haack, Haack–Adams, and Kármán ogive minimum wave-drag bodies of revolution; 7) conical flow theory; 8) reverse-flow theorems; 9) supersonic nacelle/airframe integration guidelines; 10) supersonic favorable interference predictions and concepts; 11) sonic boom prediction; 12) understanding sonic boom configuration design factors; 13) supersonic trade and sensitivity studies; and 14) baseline configuration for nonlinear design optimization.

Let us examine the fundamental differences in the results of linear theory analysis tools and in the results of corresponding nonlinear CFD analysis. Linear theory underestimates compression pressures and overestimates expansion pressures. In addition, linear theory disturbances are propagated along freestream Mach lines and therefore may not adequately predict shock formations. Linear theory with planar boundary conditions does not predict interferences between lift and volume. These differences typically are not significant effects for long, slender, thin configurations at low lift coefficients, which correspond to the geometric characteristics of low-drag supersonic configurations.

Linear theory equations as well as related direct solution formulations can provide direct insights and understanding into the effects of geometry on the nature of the flow phenomena. Because of

Presented as Paper 0132 at the 46th AIAA Aerospace Sciences Meeting and Exhibit, Reno, NV, 7–10 January 2008; received 18 December 2008; accepted for publication 8 May 2009. Copyright © 2009 by The Boeing Company. Published by the American Institute of Aeronautics and Astronautics, Inc., with permission. Copies of this paper may be made for personal or internal use, on condition that the copier pay the \$10.00 per-copy fee to the Copyright Clearance Center, Inc., 222 Rosewood Drive, Danvers, MA 01923; include the code 0021-8669/09 and \$10.00 in correspondence with the CCC.

*Engineer/Scientist and Technical Fellow, Enabling Technology and Research, Boeing Commercial Airplanes, P.O. Box 3707, Mail Stop 67-LF, Member AIAA.

[†]Private communication with R. T. Jones, about 1975.

the general ease of application and consistency of results, linear theory is often used for both sensitivity and trade studies. Linear theory can also be used to generate the large amount of data required for performance studies.

Linear theory as discussed in this paper is linear potential-flow theory with planar boundary conditions. Consequently, it is easy to incorrectly apply the theory by application to configurations for which planar boundary conditions are not appropriate or in situations in which viscous effects become significant. It is therefore important to understand the limitations of linear theory and to use discretion when applying the theory so that the solutions are physically meaningful. Properly used linear theory can predict the drag characteristics of well-behaved configurations quite accurately.

Perhaps one of the most powerful attributes of linear theory is the superposition of fundamental solutions. This allows the separation of volume effects and lifting on aerodynamic forces. This property also allows superimposing influences of component parts of an aircraft to obtain the total forces on the aircraft. Superposition is the fundamental ingredient of the methodology presented in this paper.

Early U.S. SST development studies, such as those shown in Fig. 1, have confirmed that linear theory aerodynamic designs that satisfy the set of pressure-coefficient-limiting real-flow design criteria described in [5,6] achieve the theoretical inviscid drag levels and the friction drag in the wind tunnel. The figure on the left is a comparison of the drag polar predicted by linear theory

with The Boeing Company test data for U.S. SST model 733-290. This was a linear-theory-optimized design of the configuration that allowed Boeing to win the SST design development Government contract. The friction drag CD_F was computed by the T^* method [7]. The volume wave drag CD_W was calculated by a Boeing-developed zero-lift wave-drag program that was the basis for the NASA wave-drag program [8]. The drag due to lift CD_L was calculated using the Boeing/NASA system of supersonic and analysis programs [9]. The linear theory prediction agrees very well with the test data.

The figure on the right is a comparison of the linear theory predictions with test data for the U.S. SST model 733-390. This was a linear design of the last variable-sweep configuration that Boeing studied before the final switch to the U.S. SST double-delta configuration, B2707-300. The same drag prediction methods were used as for the 733-290 configuration. Again, the linear theory prediction agrees very well with the test data. The designs developed by linear theory designs were heavily constrained by the real-flow constraints [5,6] and are therefore considered to be on the conservative side in terms of the aerodynamic performance. Hence, it is not surprising that the inviscid predictions of drag match the wind-tunnel test data.

Force calculations obtained with the inviscid and viscous CFD and with linear theory are compared with wind-tunnel test data at Mach 2.4 in Fig. 2 for two refined linear theory designs developed during the HSCT program.

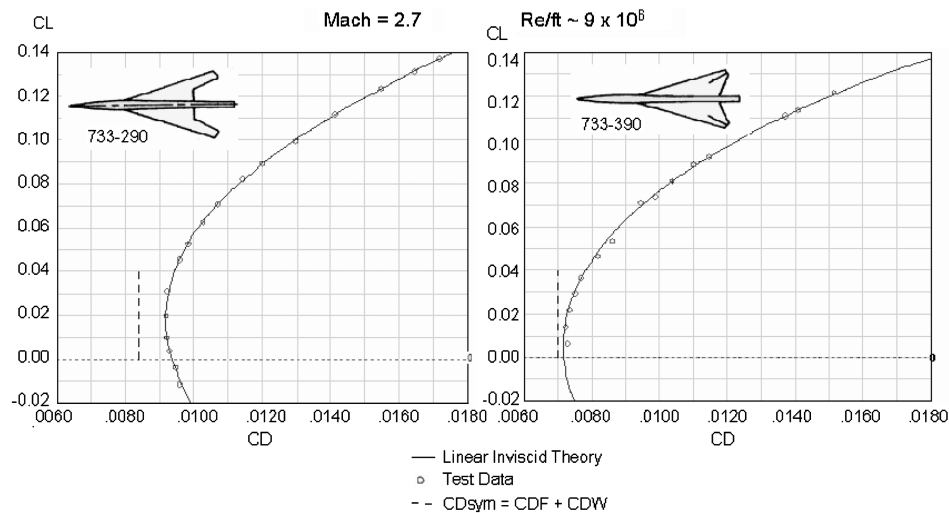


Fig. 1 Early SST linear-theory-optimized configurations test vs theory comparisons.

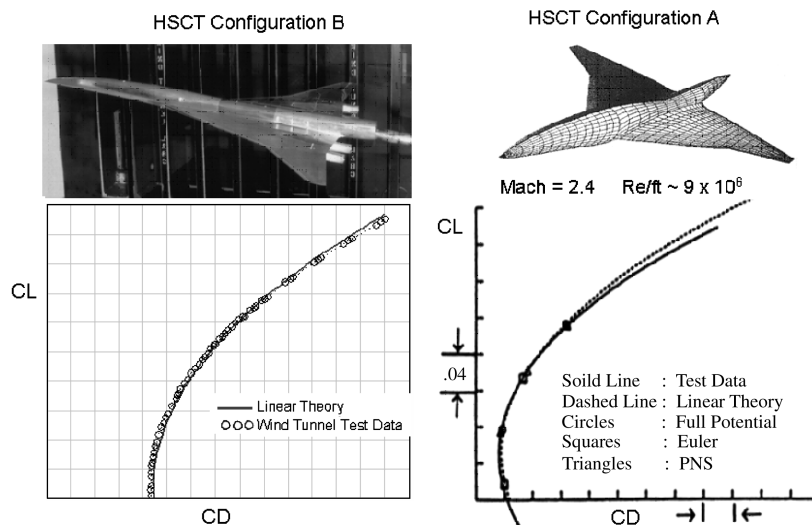


Fig. 2 Typical HSCT configurations drag polars at Mach 2.4.

The inviscid codes included linear theory, the TRANAIR full potential code, and a parabolized Euler code. The viscous analyses were obtained with a parabolized Navier–Stokes (PNS) code. Flat-plate skin-friction drag estimates were added to the inviscid CFD drag calculations and to the linear theory and Euler predictions to obtain the total aerodynamic drag. The viscous and inviscid lift and drag predictions all agree quite well with the test data. The linear theory drag predictions depart from the test data at the higher lift coefficient above the design condition.

These various test versus theory comparisons illustrate that linear theory as used in this paper can provide accurate assessments of the aerodynamic forces near the 1 *g* cruise conditions that typically correspond to the design optimization conditions. These results, together with extensive experience on the HSCT program, indicate that a good initial linear-theory-optimized design can provide the basis for developing nonlinear CFD-optimized designs.

III. Supersonic-Drag Components

The drag components of a slender supersonic configuration flying at supersonic speeds consists primarily of friction drag, wave drag due to volume, wave drag due to lift, induced drag, and other miscellaneous drag items, as shown in Fig. 3.

The friction drag is typically equal to flat-plate skin-friction drag on all of the component surfaces. The friction drag therefore depends primarily on the wetted area. The volume wave drag of a slender supersonic-type configuration, to a first order, varies with the overall volume of the configuration squared divided by the configuration length raised to the fourth power. The induced drag varies with the ratio of lift over wing span squared. The wave drag due to lift varies with lift over the streamwise length of the lifting surface squared. The wave drag due to lift vanishes as the supersonic Mach number approaches 1. It is evident that for low drag, supersonic configurations tend to be long, thin, and slender. The higher the cruise speed, the more slender the lowest-drag configuration.

The most common way to calculate drag is to sum the forces acting normal to the surface and the forces acting tangential to the surface, as shown in Fig. 4. The net drag force acting normal to the surface is

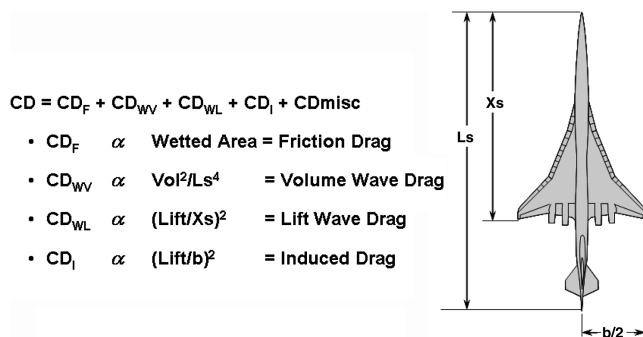


Fig. 3 Supersonic-drag components.

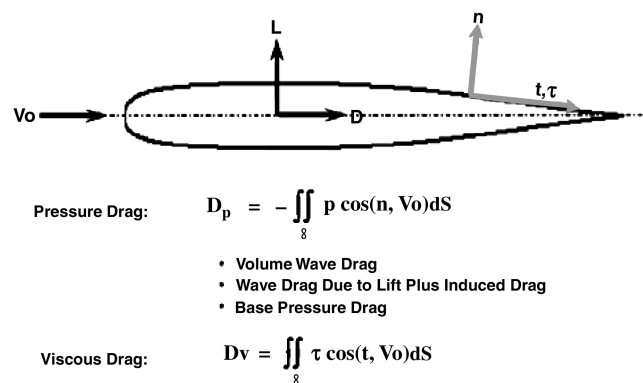


Fig. 4 Near-field calculation approach.

known as pressure drag. The forces acting tangential to the surface results from the action of viscosity and is called viscous drag or skin friction. The pressure drag is equal to the integral of the surface pressure times the cosine of the angle between the surface local outward normal and the freestream velocity direction. The viscous drag is equal to the integral of the local shear stress times the cosine of the angle between the local surface slope and the freestream velocity direction. The process of calculating forces by integration of the surface pressures and shear stress over the surface is commonly called near-field theory. This is the process typically used in nonlinear CFD codes.

The near-field linear theory approach has a number of both positive and negative features, as well as a number of negative features [10].

The near-field approach has been used to develop the conventional methods for linear theory wing camber/twist optimization. The distributions of basic lift, drag and interference forces can be determined. The nature of the flow can be judged from the surface pressure distributions. It is possible to include real-flow-limiting criteria in the design processes. Semi-empirical corrections can be included to provide useful hybrid design and analysis methods. It is also possible to incorporate higher-order corrections to the basic theory. The near-field methods most often require sophisticated numerical methods to evaluate the solution integrals. Often special care is necessary to properly account for the leading-edge forces. Although these are normally transparent to the user, they can affect the numerical accuracy of the solution. Unless the physical and mathematical limitations are known and understood, it is easy to misuse the theory and the methods. Because of the linearized boundary conditions, the analysis configurations must be planar. It is possible and often necessary to properly account for interference effects for nonplanar component arrangements such as wing/nacelle interactions with slight modifications to the theory.

An alternate way to calculate the drag of a configuration is to use a far-field theory approach shown in Fig. 5. In this approach, the drag of the configuration is determined from streamwise momentum change, through a control volume containing the configuration. The control volume is typically cylindrical. The upstream end, S1, has only freestream undisturbed flow passing through it. The downstream surface, S3, is located far enough downstream of the configuration that the pressure-induced flowfield becomes essentially two-dimensional. This is often called the Trefftz plane. The momentum change between side S1 and side S3 is due primarily to the friction drag and the induced drag. Miscellaneous drag items such as wake drag, base drag, and excrescence drag are also related to the momentum changes between S1 and S3.

The cylindrical sides are many body lengths away. At subsonic Mach numbers the flow becomes parallel to the sides of the cylinder, and hence there is no flow through this surface and hence no momentum change. At supersonic speeds, because of the shock waves and the expansion waves generated by the configuration, there is mass flow in and out of the cylinder through the sides. The streamwise momentum associated with this mass flow across the sides of the cylinder is called the wave drag. Because the shock wave structure around a supersonic configuration can change with angle of attack, the wave drag can also vary with angle of attack. Hence, the wave drag consists of the wave drag due to the volume distribution of the configuration and the variation of wave drag with lift, which is called wave drag due to lift. The far-field linear theory has a number of both positive and negative features [10].

On the positive side, the mathematical formulations of far-field theory are rather easy and have no difficulty in dealing with linear theory leading-edge forces. The far-field codes provide an easy and consistent approach to evaluate the volume wave drag of a configuration. The far-field wave-drag method provides a simple and direct method for body area-rule design optimization. Calculation of either induced drag or wave drag to lift by a far-field method requires that the lift distribution be known. Consequently, this method is not normally used to compute drag due to lift, because the near-field method would have to be used initially to obtain the lift distribution.

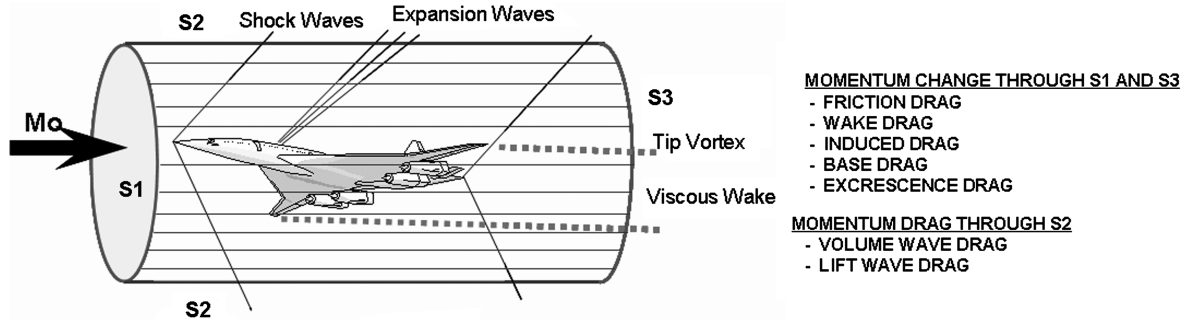


Fig. 5 Far-field drag calculation approach.

Hence, the drag due to lift would already be available from the near-field analysis.

On the negative side, the far-field optimum designs cannot be directly judged to assess the potential for success of a particular design. As is the case with any linear theory, it is easy to misuse the theory and the methods. The far-field wave-drag method essentially requires that the configuration be planar and symmetric. However, it is possible to use images to allow the meaningful analysis of nonplanar arrangements such as wing/nacelles. More extensive discussions of supersonic wave drag are contained in [10].

IV. Far-Field Supersonic Wave-Drag Calculation

As previously mentioned, the wave drag of a supersonic configuration is equal to the change in streamwise momentum due to the mass flow into and out of the side of the control volume. Lomax and Heaslet [11,12], Lomax [13], and Jones [14] showed that the momentum loss through the cylindrical sides of the control volume could be calculated as the wave drag of a series of equivalent-volume bodies. The streamwise area distributions of the equivalent bodies are determined by normal projections of the total local area of the configuration cut by oblique cutting planes through the analysis configuration at each streamwise station. The cutting planes are tangent to the freestream Mach cones, as shown in Fig. 6. The cutting planes are identified by the tangency angle θ , as shown in the figure. The $\theta = 90^\circ$ deg cutting plane is tangent to the top of the Mach fore cone. This defines the moment loss through the thin streamwise strip on top of the control volume. The $\theta = 0^\circ$ deg cutting plane is tangent to the side of the Mach cone and defines the loss of momentum through the thin strip on the side of the control volume. The cutting planes identified by values of θ between 0 and 90 deg define the

momentum loss in the streamwise strips around the cylinder between the top and the side. For a symmetric configuration, the momentum loss is symmetric in all quadrants. The total wave drag of the configuration is equal to the integrated sum of the momentum losses around the surface of the control volume, as shown in Eq. (1):

$$\frac{Dw}{q} = -\frac{1}{4\pi^2} \int_0^{2\pi} d\theta \int_0^{l(\theta)} \int_0^{l(\theta)} A''(x, \theta) A''(\xi, \theta) l_n |x - \xi| dx d\xi \quad (1)$$

The equation that defines the various cutting planes is

$$x - \beta y \cos \theta - \beta z \sin \theta = x_0 \quad (2)$$

where $\beta = \sqrt{M^2 - 1}$, and $A(x, \theta)$ is the equivalent body area distribution determined for the cutting plane θ .

It is well known that the Sears–Haack body is the minimum wave-drag body of revolution for a given volume at supersonic speeds [10]. Consequently, the lowest wave drag for any planar-type configuration would occur if every $A(\theta, x)$ area distribution in Eq. (1) had an area distribution corresponding to that of a Sears–Haack body. This is not a feasible situation for any wing planform other than a yawed elliptic wing. Therefore, the drag level associated with each $A(\theta, x)$ area distribution with an area distribution corresponding to that of a Sears–Haack body defines the absolute lower bound but unachievable wave-drag level for a general configuration with a specified volume.

The wave drag of a configuration can be easily calculated using the supersonic area-rule theory programs described in [6,7]. Figure 7 shows results of wave-drag calculations for a supersonic wing/body configuration at Mach 2.4. The wave-drag distribution around the

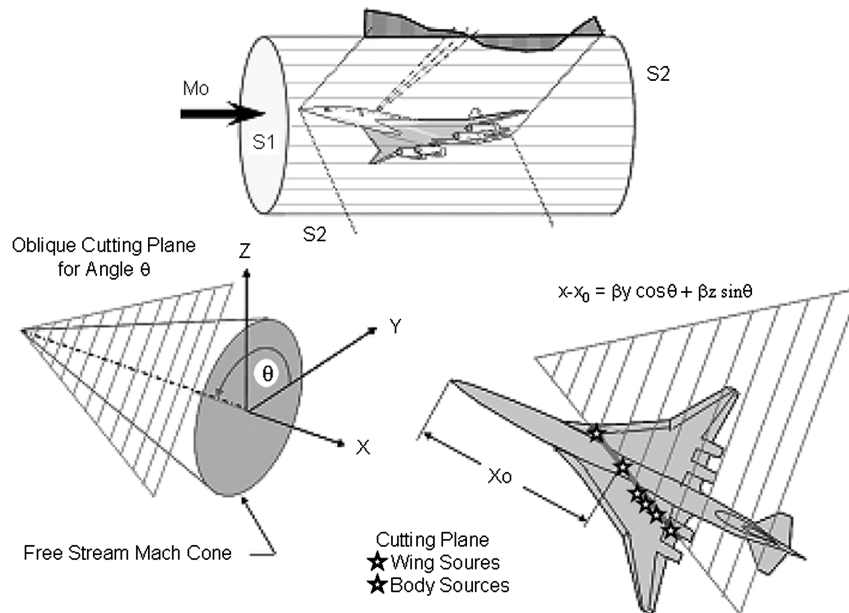


Fig. 6 Far-field wave-drag calculation.

configuration is shown along with the Mach 1 drag distribution. The maximum drag occurs for $\theta = +90$ deg and -90 deg, corresponding to above and below the configuration, respectively. The drag at these stations is equal to that at Mach 1. Some of the combined area distribution plots are shown for different angular stations around the configuration. At the higher Mach number, the angular distribution rapidly decreases to a minimum off to the side of the configuration. This is associated with the peak of the wing area distribution being reduced and the wing volume spread over a longer length.

V. Class-Function/Shape-Function Transformation Method Analytic Representation of a Wing for Design Optimization

For aerodynamic design optimization, it is very desirable to limit the number of the geometric design variables. In [1], a fundamental parametric airfoil geometry representation method was presented. The method includes the introduction of a geometric class-function/shape-function transformation technique such that round-nose/sharp-aft-end geometries as well as other classes of geometries can be represented exactly by analytic well-behaved and simple mathematical functions with easily observed physical features. The fundamental parametric geometry representation method was shown to describe an essentially limitless design space composed entirely of analytically smooth geometries. The class-function/shape-function methodology was extended [2,3] to more general three-dimensional applications such as wing, body, ducts, and nacelles. It was shown that a general 3-D geometry can be represented by a distribution of fundamental shapes and that the class-function/shape-function methodology can be used to describe the fundamental shapes as well as the distributions of the fundamental shapes. With this very robust, versatile, and simple method, a 3-D geometry is defined in a design space by the distribution of class functions and the shape functions. This design-space geometry is then transformed into the physical space in which the actual geometry is defined. The concept of analytic scalar definitions using composite-wing surfaces was also presented. The composite-wing shapes can be used for design optimization and parametric design studies.

One of the objectives of the studies presented in this paper was to evaluate the usefulness of the scalar wing concept for design optimization. A brief description and review of the CST

methodology will be shown, because knowledge of this information is essential to the understanding of the use of the methodology that is presented in the present paper.

The CST method was originally developed to provide a mathematically efficient representation of a round-nose airfoil. For a round-nose airfoil described in a fixed Cartesian coordinate system, the slopes and second derivatives of the surface geometry are infinite at the nose, and large changes in curvature occur over the entire airfoil surface. The mathematical definition of a round-nose airfoil is therefore a rather complex nonanalytic function with singularities in all derivatives at the nose. Consequently, a large number of x and z coordinates are typically required, along with a careful choice of interpolation techniques, to provide a mathematical or numerical description of the surfaces of a cambered airfoil.

In [1], it was shown that the surface coordinates for any airfoil with zero trailing-edge thickness can be mathematically defined as the product of two functions:

$$\zeta(\psi) = C_{N2}^{N1}(\psi) \cdot S(\psi) \quad (3)$$

where $\psi = x/c$ and $\zeta = z/c$

The term $C_{N2}^{N1}(\psi)$ is called the class function and is defined by the equation

$$C_{N2}^{N1}(\psi) = \psi^{N1} \cdot [1 - \psi]^{N2} \quad (4)$$

The class function for a round-nose airfoil with a sharp trailing edge, as shown in Fig. 8, has the class-function exponents $N1 = 0.5$ and $N2 = 1.0$. An airfoil with a sharp-nose airfoil and sharp trailing edge has the class-function exponent $N1 = N2 = 1.0$.

The term $S(\psi)$ is called the shape function and can be easily determined from any specified airfoil geometry by the equation

$$S(\psi) = \frac{\zeta(\psi)}{C_{N2}^{N1}(\psi)} \quad (5)$$

The shape-function equation that describes an airfoil is a simple well-behaved analytic equation that can be easily represented by a relatively small number of parameters. The shape function also has the unique feature that the nose radius and the boat-tail angle are directly related to the bounding values of the $S(\psi)$ function.

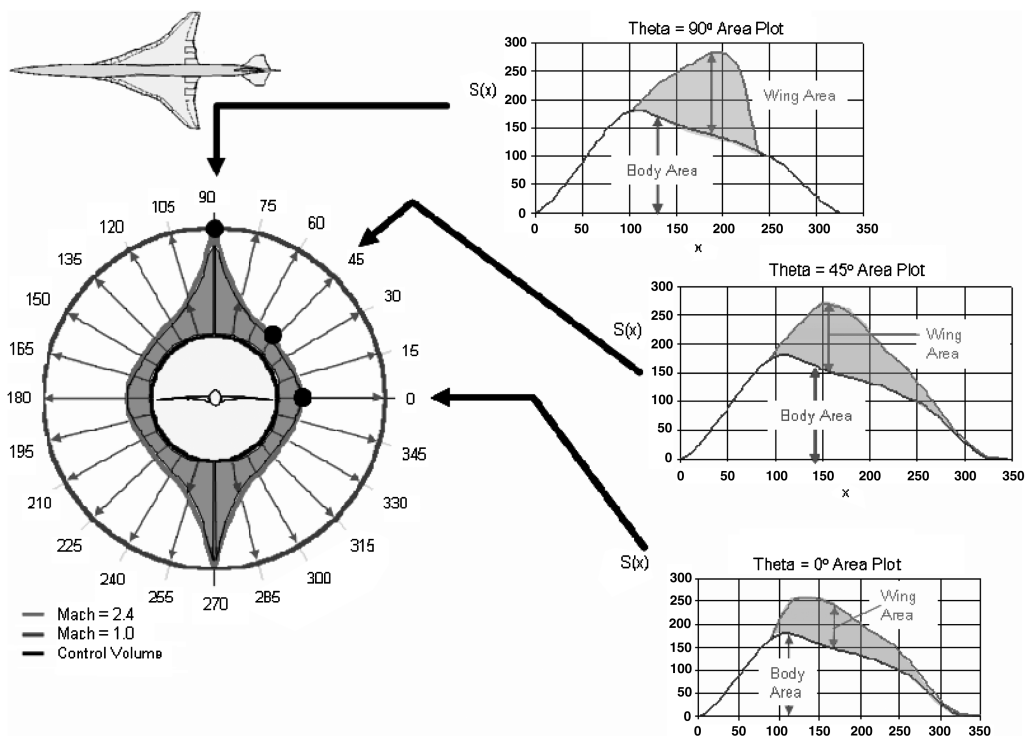


Fig. 7 Wave-drag distribution around the control volume of a typical supersonic transport configuration.

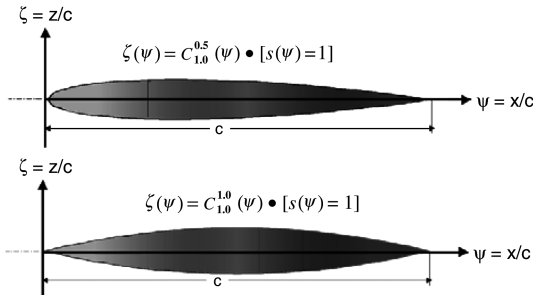


Fig. 8 Unit shape-function round-nose and sharp-nose airfoils.

The value of the shape function at $x/c = 0$ is directly related to the airfoil leading-edge nose radius R_{LE} by the relation

$$S(0) = \sqrt{2R_{LE}/c} \quad (6)$$

The value of the shape function at $x/c = 1$ is directly related to the airfoil boat-tail angle β by the relation

$$S(1) = \tan \beta + \frac{\Delta z_{TE}}{c} \quad (7)$$

An example of the transformation of an airfoil geometry to the corresponding shape function is shown in Fig. 9. The transformation of the constant- Z max-height line and the constant-boat-tail-angle line are also shown in the figure. The shape function for this example airfoil is seen to be approximately a straight line with the value at zero related to the leading-edge radius of curvature and the value at the aft end equal to the tangent of the boat-tail angle plus the ratio of trailing-edge thickness/chord length. It is readily apparent that the shape function is indeed a very simple analytic function. The areas of the airfoil that affect its drag and performance characteristics are readily visible on the shape-function curve, as shown in the figure. Furthermore, the shape function provides easy control of the airfoil critical design parameters.

The simplest of all shape functions is the constant-unit-shape function, which is defined as $S(\psi) = 1$. The unit shape function in combination with various sets of class functions define a wide variety of basic geometric shapes, shown in Table 1.

The class function defines the general classes of geometries, and the shape function is used to define specific shapes within the geometry class. The unit shape function can be decomposed into scalable component airfoils [1] by representing the shape function

with a Bernstein polynomial of order N . The representation of the unit shape function in terms of increasing orders of the Bernstein polynomials provides a systematic decomposition of the unit shape function into scalable components. This is the direct result of the partition-of-unity property, which states that the sum of the terms that make up a Bernstein polynomial of any order, over the interval of 0 to 1, is equal to 1. This means that every Bernstein polynomial represents the unit shape function. Consequently, the individual terms in the polynomial can be scaled to define an extensive variety of airfoil geometries [1].

The Bernstein polynomial of any order n is composed of the $n + 1$ terms of the form

$$S_{r,n}(x) = K_{r,n} x^r (1-x)^{n-r} \quad (8)$$

where $r = 0$ to n , and n is the order of the Bernstein polynomial.

In Eq. (9), the coefficients factors $K_{r,n}$ are binominal coefficients defined as

$$K_{r,n} \equiv \binom{n}{r} \equiv \frac{n!}{r!(n-r)!} \quad (9)$$

For any order of Bernstein polynomial selected to represent the unit shape function, only the first term defines the leading-edge radius and only the last term defines the boat-tail angle. The other in-between terms are shaping terms that affect neither the leading-edge radius nor the trailing-edge boat-tail angle. Examples of decompositions of the unit shape function using various orders of Bernstein polynomials are shown in Fig. 10, along with the corresponding composite airfoils that are obtained by multiplying the component shape function by the class function.

The technique of using Bernstein polynomials to represent the shape function of an airfoil in reality defines a systematic set of component airfoil shapes that can be scaled to represent a variety of airfoil geometries, as illustrated in Fig. 11.

The method of using Bernstein polynomials to represent an airfoil has the following unique and very powerful properties [1]:

- 1) This airfoil representation technique captures the entire design space of smooth airfoils.
- 2) Every airfoil in the entire design space can be derived from the unit shape-function airfoil.
- 3) Every airfoil in the design space is therefore derivable from every other airfoil.

Using Bernstein polynomials, the general equation for the shape function of any symmetric airfoil can be expressed as

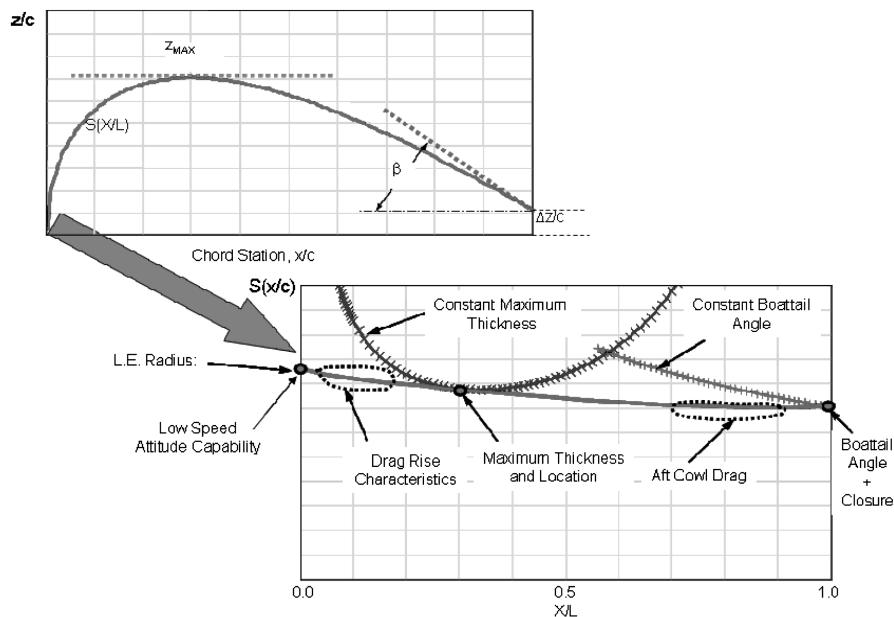









Fig. 9 Example of an airfoil geometric transformation.

Table 1 Various classes of geometries defined by the class function and unit shape function

Class function equation	Geometry description	Examples
$\zeta(\psi) = C_{1.0}^{0.5}(\psi)$	Defines a NACA-type round-nose and pointed-aft-end airfoil.	
$\zeta(\psi) = C_{0.5}^{0.5}(\psi)$	Defines an elliptic airfoil or body of revolution.	
$\zeta(\psi) = C_{1.0}^{1.0}(\psi)$	Defines a biconvex airfoil or an ogive body.	
$\zeta(\zeta) = C_{0.75}^{0.75}(\psi)$	Defines the radius distribution of a Sears–Haack body.	
$\zeta(\psi) = C_{0.25}^{0.75}(\psi)$	Defines a low-drag projectile.	
$\zeta(\psi) = C_{0.001}^{1.0}(\psi)$	Defines a cone or wedge airfoil.	
$\zeta(\psi) = C_{0.001}^{0.001}(\psi)$	Defines a rectangle or circular rod.	

$$S(\psi) = \sum_{i=0}^{Nx} Ax_i \cdot S_i(\psi) \quad (10)$$

where Nx is the order of the selected Bernstein polynomial.

The equation defining the airfoil coordinates is

$$\zeta(\psi) = C_{N2}^{N1}(\psi) \cdot S(\psi) = \sum_{i=0}^{Nx} Ax_i \cdot C_{N2}^{N1}(\psi) \cdot S_i(\psi) \quad (11)$$

The coefficients Ax_i can be determined by a variety of techniques, depending on the objective of the particular study. Some examples include variables in a numerical design optimization application, least-squares fit to match a specified geometry, and parametric shape variations.

A 3-D wing can be considered to be a distribution of airfoils across the wing span. Sectional applications of the shape function can thus produce an analytic shape-function surface describing the entire wing. It was shown in [2] that the shape-function surface for a complete wing surface can be obtained by first representing the root airfoil shape function by a Bernstein polynomial of a specified order. The complete wing shape-function surface can then be defined by expanding the coefficients of the chordwise Bernstein polynomial in the spanwise direction using any appropriate numerical technique. The surface definition of the wing is then obtained by multiplying the

shape-function surface by the wing class function. This, in essence, provides an analytic scalar definition of any wing surface.

In this paper, we will use the Bernstein polynomial formulation to represent the streamwise airfoil shapes by a set of composite airfoils and to describe the spanwise variation of the magnitude of each composite airfoil across the wing span. The mathematical description of the wing surface is easily obtained by expanding the airfoil Ax_i coefficients in the spanwise direction using Bernstein polynomials of order Ny as

$$Ax_i(\eta) = \sum_{j=0}^{Ny} B_{i,j} Sy_j(\eta) \quad (12)$$

where

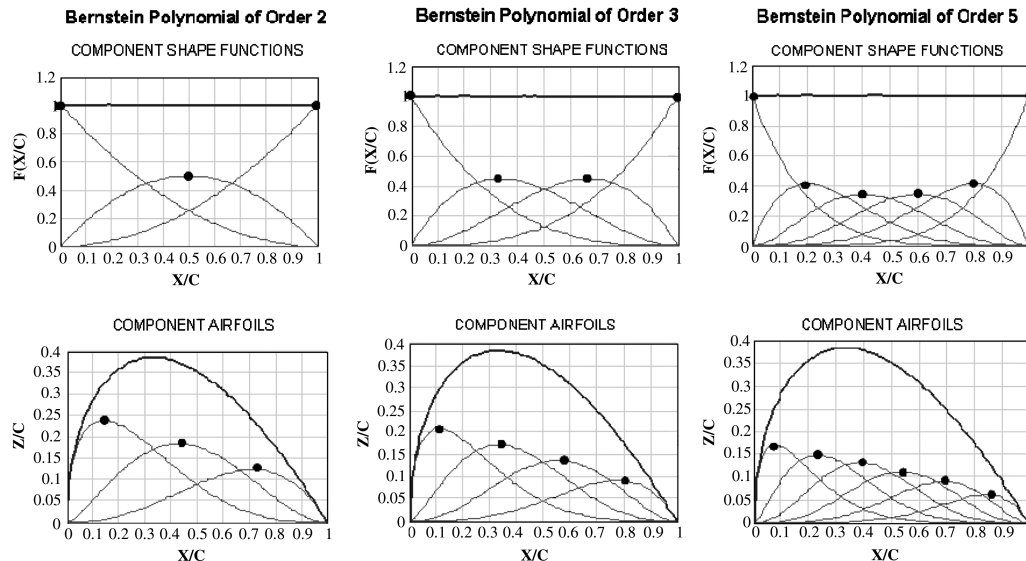
$$Sy_j(\psi) = Ky_j \eta^j (1 - \eta)^{Ny-j} \quad \text{for } j = 0 \text{ to } Ny \quad (13)$$

and

$$Ky_j \equiv \binom{Ny}{j} \equiv \frac{Ny!}{j!(Ny-j)!} \quad (14)$$

The symmetric wing surface is then defined by

$$\zeta(\psi, \eta) = \sum_{i=0}^{Nx} \sum_{j=0}^{Ny} [B_{i,j} Sy_j(\eta) \{C_{N2}^{N1}(\psi) Sx_i(\psi)\}] \quad (15)$$

**Fig. 10** Bernstein polynomial provides natural shapes.

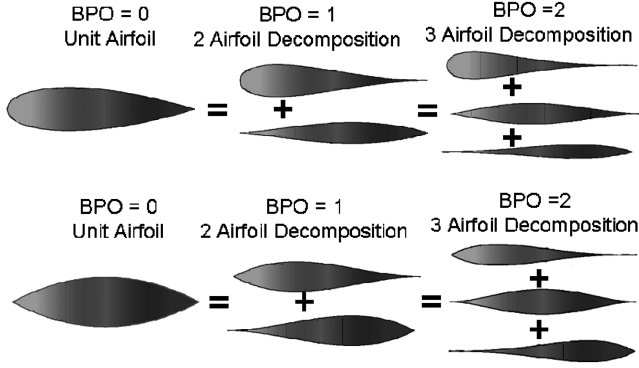


Fig. 11 Example component airfoils.

The coefficients $B_{i,j}$ will be the design optimization for the studies described in this paper.

This process of defining a wing geometry may be considered a scalar loft of a wing, where every point on the wing surface is defined as accurately as desired and the points are all connected by the analytic equations. This is in contrast to the usual wing definition of a vector loft of a wing, which is defined as ordered sets of x , y , and z coordinates and rules that describe how to connect adjoining points. The common approach used in most vector lofts is to connect adjacent points along constant-span stations and along constant-percent-chord lines.

In Eq. (15), each term $\zeta_{ij}(\psi, \eta) = C_{N2}^{N1}(\psi)Sx_i(\psi)Sy_j(\eta)$ defines a composite-wing geometry formed by the i th component airfoil shape with the j th spanwise variation.

The total wing is then represented by a total of Nt scalable composite-wing elements, where

$$Nt = (Nx + 1) \cdot (Ny + 1) \quad (16)$$

VI. FCE Wing Representation as Composite Elements

The FCE optimization method will be formulated using the previously discussed CST analytic wing representation method. The wing will be represented as a set of composite-wing elements. First select the order of the Bernstein polynomial Nx to define the set of composite airfoil shapes. Then select the order of the Bernstein polynomial Ny to define the spanwise variations of the composite airfoil shapes. The total number of resulting composite-wing shapes is given by Eq. (16). The total wing surface is then defined by

$$\zeta(\psi, \eta) = \sum_{j=0}^{Ny} Sy_j(\eta) \sum_{i=0}^{Nx} B_{i,j}[C_{1,0}^{0.5}(\psi)Sx_i(\psi)] \quad (17)$$

It is convenient to convert this matrix representation of the wing shape into an equivalent vector definition. This can be achieved using the following transformation process. An i, j matrix can be converted into a k element vector using the transformation.

Define

$$\begin{aligned} zz_{k,0} &\triangleq \text{trunc}\left(\frac{k}{Ny + 1}\right) \quad \text{and} \\ zz_{k,1} &\triangleq k - (Ny + 1) \cdot \text{trunc}\left(\frac{k}{Ny + 1}\right) \end{aligned} \quad (18)$$

where $k = 0$ to $Nt - 1$.

Let

$$ik_k = zz_{k,0} \quad \text{and} \quad jk_k = zz_{k,1}$$

By substitution,

$$\zeta(\psi, \eta)_k \equiv \zeta(\psi, \eta)_{ik_k, jk_k} \quad (19)$$

Each of the k composite wings has a corresponding wing volume V_k that is obtained by integration of the corresponding composite-

wing thickness distribution over the wing planform area. These integrated volumes are obtained as part of the wave-drag analysis of each composite wing.

The total base-wing volume is given by

$$V_{\text{base}} = \sum_{k=1}^{Nt} V_k$$

As previously shown in Eq. (1), the wave drag of an isolated wing can be calculated from the area distribution of the wing as

$$\frac{D}{q} = -\frac{1}{4\pi^2} \int_0^{2\pi} d\theta \int_0^{l(\theta)} \int_0^{l(\theta)} A''(x, \theta) A''(\xi, \theta) \ell_n |x - \xi| dx d\theta$$

The total wing area can be represented as the sum of the areas of the fundamental wing elements as

$$A(x, \theta) = \sum_{i=1}^{Nt} A_i(x, \theta) \quad (20)$$

By substitution,

$$\begin{aligned} CDw &= \frac{1}{2\pi S_{\text{ref}}} \int_0^{2\pi} \int_0^{l(\theta)} \int_0^{l(\theta)} \sum_{i=1}^{Nt} A_i''(x, \theta) \sum_{j=1}^{Nt} A_j''(x, \xi) \ell_n |x \\ &\quad - \xi| dx d\xi d\theta \end{aligned} \quad (21)$$

Interchanging the order of integration and summation yields

$$\begin{aligned} CDw &= \frac{1}{2\pi S_{\text{ref}}} \sum_{i=1}^{Nt} \sum_{j=1}^{Nt} \int_0^{2\pi} \int_0^{l(\theta)} \int_0^{l(\theta)} A_i''(x, \theta) A_j''(x, \xi) \ell_n |x \\ &\quad - \xi| dx d\xi d\theta \end{aligned} \quad (22)$$

The total wave drag can then be written as the double sum

$$CDw = \sum_{i=1}^{Nt} \sum_{j=1}^{Nt} CD_{ij} \quad (23)$$

where

$$CD_{ij} \triangleq \frac{1}{2\pi S_{\text{ref}}} \int_0^{2\pi} \int_0^{l(\theta)} \int_0^{l(\theta)} A_i''(x, \theta) A_j''(x, \xi) \ell_n |x - \xi| dx d\xi d\theta \quad (24)$$

For $i = j$, CD_{ii} is the drag of fundamental element $A_i A_i$. For $i \neq j$: $CD_{ij} + CD_{ji}$ is the interference drag between element A_i and element A_j . For simplicity, we will use the notation

$$CD_{ij} \triangleq CD_{ij} + CD_{ji} \quad \text{for } i \neq j \quad (25)$$

and

$$CD_{ii} \triangleq CD_{ii} \quad \text{for } i = j \quad (26)$$

Therefore, the total wave drag is equal to the sum of the wave drag of each isolated volume component plus the mutual interference drag between each pair of volume elements. The isolated drag of any of the fundamental elements can be obtained by computing [7] the wave drag in which the wing analysis geometry is represented by the single-component-wing geometry. To calculate the mutual interference drag between any of the two wing elements, we will use the identity

$$(A_i + A_j)^2 \equiv (A_i)^2 + 2A_i A_j + (A_j)^2 \quad (27)$$

and therefore

$$2A_i A_j \equiv (A_i + A_j)^2 - (A_i)^2 - (A_j)^2$$

Consequently,

	A ₁	A ₂	A ₃	A ₄	A ₅	A ₆
A ₁	$\hat{C}\hat{D}_{11}$	$2\hat{C}\hat{D}_{12}$	$2\hat{C}\hat{D}_{13}$	$2\hat{C}\hat{D}_{14}$	$2\hat{C}\hat{D}_{15}$	$2\hat{C}\hat{D}_{16}$
A ₂		$\hat{C}\hat{D}_{22}$	$2\hat{C}\hat{D}_{23}$	$2\hat{C}\hat{D}_{24}$	$2\hat{C}\hat{D}_{25}$	$2\hat{C}\hat{D}_{26}$
A ₃			$\hat{C}\hat{D}_{33}$	$2\hat{C}\hat{D}_{34}$	$2\hat{C}\hat{D}_{35}$	$2\hat{C}\hat{D}_{36}$
A ₄				$\hat{C}\hat{D}_{44}$	$2\hat{C}\hat{D}_{45}$	$2\hat{C}\hat{D}_{46}$
A ₅					$\hat{C}\hat{D}_{55}$	$2\hat{C}\hat{D}_{56}$
A ₆						$\hat{C}\hat{D}_{66}$

Fig. 12 Wave-drag matrix for a six-composite-element wing.

$$\hat{C}\hat{D}_{ij} = CD(A_i + A_j) - CD(A_i) - CD(A_j) \quad (28)$$

The interference drag between any of two wing elements i and j can therefore be determined by calculating the drag of a wing composed of the sum of the two wing components i and j and then subtracting the drags of the individual elements. The total wing drag in terms of the drags of the fundamental elements is equal to

$$CD_W = \sum_{i=1}^{N_t} \sum_{j \neq i, j=1}^{N_t} \hat{C}\hat{D}_{ij} w_{ij} \quad (29)$$

The total number of individual required composite-wing wave-drag analyses N_{cal} equals

$$N_{\text{cal}} = \frac{N^2 + N}{2} \quad (30)$$

An example of the far-field wave-drag component matrix for a six-composite-element wing is shown in Fig. 12.

VII. Isolated-Wing Optimization

To formulate the wing optimization process, we will introduce the to-be-determined composite-wing thickness scaling factors S_i , so that the i th composite-wing element thickness distribution and its corresponding elementary volume scale linearly with S_i .

The total scaled-wing volume vol is therefore

$$\text{vol} = V_{\text{base}} V_R = \sum_{i=1}^{N_t} S_i V_i \quad (31)$$

where V_{base} is the original unscaled-wing volume and V_R is the ratio of the desired wing volume to the original wing volume. The scaled-wing half-thickness distribution equation becomes

$$\xi(\psi, \eta) = \sum_{i=1}^{N_t} s_i \xi_i(\psi, \eta) \quad (32)$$

The wing area distribution becomes

$$A(x, \theta) = \sum_{i=1}^{N_t} s_i A_i(x, \theta) \quad (33)$$

Consequently, the scaled-wing wave drag becomes

$$CD_W = \sum_{i=1}^{N_t} \sum_{j=1}^{N_t} (s_i s_j \hat{C}\hat{D}_{ij}) \quad (34)$$

It is convenient to write the volume equation in terms of the original wing volume-fraction ratios v_i . This defines the fraction of the total wing volume that is due the composite-wing element i :

$$v_i \triangleq \frac{V_i}{V_{\text{base}}} \quad (35)$$

The total volume equation becomes

$$V_R = \sum_{i=1}^{N_t} \frac{S_i V_i}{V_{\text{base}}} = \sum_{i=1}^{N_t} S_i v_i \quad (36)$$

Let

$$\tilde{D}_{ij} \equiv \frac{\hat{C}\hat{D}_{ij}}{v_i v_j} \quad (37)$$

Introduce the condensed volume-fraction scaling factor

$$k_i = S_i v_i \quad (38)$$

The wing volume equation becomes

$$V_R = \sum_{i=1}^{N_t} k_i \quad (39)$$

The wave-drag equation is

$$CD_W = \sum_{i=1}^{N_t} \sum_{j=1}^{N_t} (k_i)(k_j) \tilde{D}_{ij} \quad (40)$$

We can now define our optimization problem as determining the unknown coefficients k_i to minimize the wave drag in Eq. (40) for a given volume ratio V_R defined by Eq. (39).

The volume equation can be written as a linear constraint equation as

$$\Phi_V = 0 = V_R - \sum_{i=1}^N k_i \quad (41)$$

The optimization problem can be formulated using Lagrange's multiplier λ_V .

Define

$$F = CD_W - \lambda_V \Phi_V \quad (42)$$

The solution for minimum wave-drag subject to the volume constraint Eq. (21) can then be determined from the system of linear equations derived from Eq. (22) as follows:

For $i = 1$ to N ,

$$\frac{\partial F}{\partial k_i} = 0 \quad \text{and} \quad \frac{\partial F}{\partial \lambda_V} = 0 \quad (43)$$

This provides the complete system of $N + 1$ linear equations to determine the $N + 1$ unknowns.

The system of linear equations to solve are

$$\frac{\partial F}{\partial k_i} = 2\tilde{D}_{ii}k_i + \sum_{j=1, j \neq i}^{N_t} \tilde{D}_{ij}k_j + \lambda_V = 0 \quad (44)$$

and

$$\frac{\partial F}{\partial \lambda_V} = \sum_{i=1}^{N_t} k_i - V_R = 0 \quad (45)$$

For example, the set of equations for a six-component-wing optimization are

$$\begin{aligned}
2\tilde{D}_{11}k_1 + \tilde{D}_{12}k_2 + \tilde{D}_{13}k_3 + \tilde{D}_{14}k_4 + \tilde{D}_{15}k_5 + \tilde{D}_{16}k_6 + \lambda_V &= 0 \\
\tilde{D}_{21}k_1 + 2\tilde{D}_{22}k_2 + \tilde{D}_{23}k_3 + \tilde{D}_{24}k_4 + \tilde{D}_{25}k_5 + \tilde{D}_{26}k_6 + \lambda_V &= 0 \\
\tilde{D}_{31}k_1 + \tilde{D}_{32}k_2 + 2\tilde{D}_{33}k_3 + \tilde{D}_{34}k_4 + \tilde{D}_{35}k_5 + \tilde{D}_{36}k_6 + \lambda_V &= 0 \\
\tilde{D}_{41}k_1 + \tilde{D}_{42}k_2 + \tilde{D}_{43}k_3 + 2\tilde{D}_{44}k_4 + \tilde{D}_{45}k_5 + \tilde{D}_{46}k_6 + \lambda_V &= 0 \\
\tilde{D}_{51}k_1 + \tilde{D}_{52}k_2 + \tilde{D}_{53}k_3 + \tilde{D}_{54}k_4 + 2\tilde{D}_{55}k_5 + \tilde{D}_{56}k_6 + \lambda_V &= 0 \\
\tilde{D}_{61}k_1 + \tilde{D}_{62}k_2 + \tilde{D}_{63}k_3 + \tilde{D}_{64}k_4 + \tilde{D}_{65}k_5 + 2\tilde{D}_{66}k_6 + \lambda_V &= 0 \\
k_1 + k_2 + k_3 + k_4 + k_5 + k_6 + 0 &= VR
\end{aligned}$$

The solution to these equations can be expressed in matrix form as

$$\begin{bmatrix} 2\tilde{D}_{11} & \tilde{D}_{12} & \tilde{D}_{13} & \cdots & \tilde{D}_{1N} & 1 \\ \tilde{D}_{21} & 2\tilde{D}_{22} & \tilde{D}_{23} & \cdots & \tilde{D}_{2N} & 1 \\ \tilde{D}_{31} & \tilde{D}_{32} & 2\tilde{D}_{33} & \cdots & \tilde{D}_{3N} & 1 \\ \vdots & \vdots & \vdots & \ddots & \vdots & \vdots \\ \tilde{D}_{N1} & \tilde{D}_{N2} & \tilde{D}_{N3} & \cdots & 2\tilde{D}_{NN} & 1 \\ 1 & 1 & 1 & 1 & 1 & 0 \end{bmatrix} \begin{bmatrix} k_1 \\ k_2 \\ k_3 \\ \vdots \\ k_N \\ \lambda_V \end{bmatrix} = \begin{bmatrix} 0 \\ 0 \\ 0 \\ \vdots \\ 0 \\ V_R \end{bmatrix}$$

The matrix equations can be written in condensed form as

$$[D][k] = [R] \quad (46)$$

The solution for the unknowns k_i and λ_V is easily obtained by matrix inversion as

$$[D][R]^{-1} = [k] \quad (47)$$

The solution to the equations is given by the values of k_i . The optimized composite-wing scaling factors are calculated from k_i as

$$s_i = k_i \frac{V_{\text{base}}}{V_i} \quad (48)$$

The optimum z/c distribution is calculated from Eq. (32) and the corresponding minimum wave drag is obtained from Eq. (34).

VIII. Including Fuselage and Nacelle Interference Effects

The drag of a wing/body configuration can be calculated using Eq. (1) with the wing/body combined area distribution. The area distributions consist of the wing area A_W plus the body area A_B distributions:

$$At(x, \theta) = A_W(x, \theta) + A_B(x) \quad (49)$$

Substituting Eq. (49) into Eq. (1) indicates that the wing/body drag consists of three components:

The drag of the isolated wing is

$$\begin{aligned}
CDw_{\text{wing}} &= \frac{1}{2\pi S_{\text{ref}}} \int_0^{2\pi} \int_0^{l(\theta)} \int_0^{l(\theta)} A''_W(x, \theta) A''_W(\xi, \theta) l_n |x - \xi| dx d\xi d\theta \\
&\quad - \xi | dx d\xi d\theta \quad (50)
\end{aligned}$$

The drag of the isolated body is

$$CDw_{\text{body}} = \frac{1}{S_{\text{ref}}} \int_0^{L_B} \int_0^{L_B} A''_B(x) A''_B(\xi) l_n |x - \xi| dx d\xi \quad (51)$$

Wing/body interference drag is

$$\begin{aligned}
CDw_{\text{WBint}} &= \frac{2}{2\pi S_{\text{ref}}} \int_0^{2\pi} \int_0^{l(\theta)} \int_0^{l(\theta)} A''_B(\xi) A''_W(x, \theta) l_n |x - \xi| dx d\xi d\theta \\
&\quad - \xi | dx d\xi d\theta \quad (52)
\end{aligned}$$

The wing area distribution can be represented as the sum of the areas of the fundamental wing elements:

$$Aw(x, \theta) = \sum_{i=1}^{N_t} A_i(x, \theta) \quad (53)$$

The wing/body interference drag then becomes

$$\begin{aligned}
CDw_{\text{WBint}} &= \frac{2}{2\pi S_{\text{ref}}} \int_0^{2\pi} \int_0^{l(\theta)} \int_0^{l(\theta)} A''_B(\xi) \sum_{i=1}^{N_t} A''_i(x, \theta) l_n |x - \xi| dx d\xi d\theta \\
&\quad - \xi | dx d\xi d\theta \quad (54)
\end{aligned}$$

Interchanging the order of summation and integration gives

$$\begin{aligned}
CDw_{\text{WBint}} &= \frac{1}{\pi S_{\text{ref}}} \sum_{i=1}^{N_t} \int_0^{2\pi} \int_0^{l(\theta)} \int_0^{l(\theta)} A''_B(\xi) A''_i(x, \theta) l_n |x - \xi| dx d\xi d\theta \\
&\quad - \xi | dx d\xi d\theta \quad (55)
\end{aligned}$$

Define the interference drag between the body and wing element A_i , CDw_{b_i} , as

$$CDw_{b_i} \triangleq \frac{1}{\pi S_{\text{ref}}} \int_0^{2\pi} \int_0^{l(\theta)} \int_0^{l(\theta)} A''_B(\xi) A''_i(x, \theta) l_n |x - \xi| dx d\xi d\theta \quad (56)$$

Therefore,

$$CDw_{\text{WBint}} = \sum_{i=1}^N CDw_{b_i} \quad (57)$$

The wing/body interference drag is equal to the sum of the interference drags of the body with each of the isolated-wing elements. To calculate CDw_{b_i} , use the identity

$$[A_B + A_i]^2 \equiv A_B^2 + 2A_B A_i + A_i^2 \quad (58)$$

Consequently,

$$CDw_{b_i} = CD(A_B + A_i) - CD(A_i) - CD(A_B) \quad (59)$$

The interference drag between the body and wing composite element A_i is obtained by computing the wave drag of the body with the composite-wing element and subtracting the isolated body drag CDw_{body} and the isolated drag of the composite-wing element. The total wave drag of the wing/body in terms of the wing composite elements is therefore

$$CDw = \sum_{i=1}^{N_t} \sum_{j=1}^{N_t} CD\hat{D}_{ij} + \sum_{i=1}^{N_t} CDw_{b_i} + CDw_{\text{body}} \quad (60)$$

An example of the drag matrix for a six-composite-element wing is shown in Fig. 13. The presence of the body adds a single row to the isolated-wing drag matrix.

The inclusion of the wing/body interference requires only the addition of $N + 1$ additional initial calculations to start the optimization solution. The total number of individual required element wave-drag analyses equals

	A_1	A_2	A_3	A_4	A_5	A_6
CDw_{body}	CDw_{b_1}	CDw_{b_2}	CDw_{b_3}	CDw_{b_4}	CDw_{b_5}	CDw_{b_6}
A_1	$\hat{C}\hat{D}_{11}$	$2\hat{C}\hat{D}_{12}$	$2\hat{C}\hat{D}_{13}$	$2\hat{C}\hat{D}_{14}$	$2\hat{C}\hat{D}_{15}$	$2\hat{C}\hat{D}_{16}$
A_2		$\hat{C}\hat{D}_{22}$	$2\hat{C}\hat{D}_{23}$	$2\hat{C}\hat{D}_{24}$	$2\hat{C}\hat{D}_{25}$	$2\hat{C}\hat{D}_{26}$
A_3			$\hat{C}\hat{D}_{33}$	$2\hat{C}\hat{D}_{34}$	$2\hat{C}\hat{D}_{35}$	$2\hat{C}\hat{D}_{36}$
A_4				$\hat{C}\hat{D}_{44}$	$2\hat{C}\hat{D}_{45}$	$2\hat{C}\hat{D}_{46}$
A_5					$\hat{C}\hat{D}_{55}$	$2\hat{C}\hat{D}_{56}$
A_6						$\hat{C}\hat{D}_{66}$

Fig. 13 Example of a six-composite-element wing/body drag matrix.

$$N_{\text{cal}} = \frac{N^2 + N}{2} + N + 1 \quad (61)$$

The wing/body drag equation in terms of arbitrary scaling coefficients s_i is

$$CD_W = CD_{\text{body}} + \sum_{i=1}^{N_t} \sum_{j=1}^{N_t} (s_i v_i)(s_j v_j) \frac{CD_{ij}}{v_i v_j} + \sum_{i=1}^{N_t} (s_i v_i) \frac{CD_{wb_i}}{v_i} \quad (62)$$

As previously noted,

$$\hat{D}_{ij} \triangleq \frac{CD_{ij}}{v_i v_j} \quad \text{and} \quad k_i \triangleq s_i v_i$$

Let

$$D_{wb_i} \triangleq \frac{CD_{wb_i}}{v_i} \quad (63)$$

The total wave-drag equation in terms of the to-be-determined optimization variables k_i becomes

$$CD_W = CD_{\text{body}} + \sum_{i=1}^{N_t} \sum_{j=1}^{N_t} (k_i)(k_j) D_{ij} + \sum_{i=1}^{N_t} (k_i) D_{wb_i} \quad (64)$$

We will follow the same optimization procedure with Lagrange's multipliers as for the isolated-wing case. The system of linear equations to solve to determine the optimum wing geometry in the presence of a body are

$$\frac{\partial F}{\partial k_i} = 2D_{ii}k_i + \sum_{j=1, j \neq i}^{N_t} D_{ij}k_j + (D_{wb_i} + \lambda_V) = 0 \quad (65)$$

together with the volume constraint equation:

$$\frac{\partial F}{\partial \lambda_V} = k_1 + k_2 + k_3 + k_4 \cdots + k_N - V_R = 0 \quad (66)$$

The solution equations for an example of six-composite-wing elements plus the body are

$$\begin{aligned} 2\tilde{D}_{11}k_1 + \tilde{D}_{12}k_2 + \tilde{D}_{13}k_3 + \tilde{D}_{14}k_4 + \tilde{D}_{15}k_5 + \tilde{D}_{16}k_6 + \lambda_V \\ = -D_{wb_1} \\ \tilde{D}_{21}k_1 + 2\tilde{D}_{22}k_2 + \tilde{D}_{23}k_3 + \tilde{D}_{24}k_4 + \tilde{D}_{25}k_5 + \tilde{D}_{26}k_6 + \lambda_V \\ = -D_{wb_2} \\ \tilde{D}_{31}k_1 + \tilde{D}_{32}k_2 + 2\tilde{D}_{33}k_3 + \tilde{D}_{34}k_4 + \tilde{D}_{35}k_5 + \tilde{D}_{36}k_6 + \lambda_V \\ = -D_{wb_3} \\ \tilde{D}_{41}k_1 + \tilde{D}_{42}k_2 + \tilde{D}_{43}k_3 + 2\tilde{D}_{44}k_4 + \tilde{D}_{45}k_5 + \tilde{D}_{46}k_6 + \lambda_V \\ = -D_{wb_4} \\ \tilde{D}_{51}k_1 + \tilde{D}_{52}k_2 + \tilde{D}_{53}k_3 + \tilde{D}_{54}k_4 + 2\tilde{D}_{55}k_5 + \tilde{D}_{56}k_6 + \lambda_V \\ = -D_{wb_5} \\ \tilde{D}_{61}k_1 + \tilde{D}_{62}k_2 + \tilde{D}_{63}k_3 + \tilde{D}_{64}k_4 + \tilde{D}_{65}k_5 + 2\tilde{D}_{66}k_6 + \lambda_V \\ = -D_{wb_6} \\ k_1 + k_2 + k_3 + k_4 + k_5 + k_6 + 0 = V_R \end{aligned}$$

The system of equations is shown next in matrix form:

$$\begin{bmatrix} 2\tilde{D}_{11} & \tilde{D}_{12} & \tilde{D}_{13} & \tilde{D}_{14} & \tilde{D}_{15} & \tilde{D}_{16} & 1 \\ \tilde{D}_{21} & 2\tilde{D}_{22} & \tilde{D}_{23} & \tilde{D}_{24} & \tilde{D}_{25} & \tilde{D}_{26} & 1 \\ \tilde{D}_{31} & \tilde{D}_{32} & 2\tilde{D}_{33} & \tilde{D}_{34} & \tilde{D}_{35} & \tilde{D}_{36} & 1 \\ \tilde{D}_{41} & \tilde{D}_{42} & \tilde{D}_{43} & 2\tilde{D}_{44} & \tilde{D}_{45} & \tilde{D}_{46} & 1 \\ \tilde{D}_{51} & \tilde{D}_{52} & \tilde{D}_{53} & \tilde{D}_{54} & 2\tilde{D}_{55} & \tilde{D}_{56} & 1 \\ \tilde{D}_{61} & \tilde{D}_{62} & \tilde{D}_{63} & \tilde{D}_{64} & \tilde{D}_{65} & 2\tilde{D}_{66} & 1 \\ 1 & 1 & 1 & 1 & 1 & 1 & 0 \end{bmatrix} \begin{bmatrix} k_1 \\ k_2 \\ k_3 \\ k_4 \\ k_5 \\ k_6 \\ \lambda_V \end{bmatrix} = \begin{bmatrix} -D_{wb_1} \\ -D_{wb_2} \\ -D_{wb_3} \\ -D_{wb_4} \\ -D_{wb_5} \\ -D_{wb_6} \\ V_R \end{bmatrix}$$

The solution process is the same as for the isolated-wing optimization process [Eqs. (46–48)].

The formulation of the process for optimization in the presence of the nacelles is identical to the process described earlier for including body interference effects.

IX. Adding Local Wing Thickness Constraints

An interesting feature of a linear theory optimization process is that the optimum volume-constrained solution may include regions of the wing with vanishingly small or, in some instances, negative thicknesses. This is an indication that in those regions of the wing, volume is accompanied by relatively high wave drag. In essence, this is an attempt by the linear theory to alter the wing planform. Consequently, in addition to an overall volume constraint, it is often necessary to provide the capability to impose local minimum wing thickness constraints. To accomplish this, we will define a general local depth or area constraint in terms of a desired average thickness/chord ratio at a specific station η_C and over a portion of the local chord $\Delta x/c$, which is defined as

$$\Delta\psi c = \psi_{\text{aft}} - \psi_{\text{fwd}} \quad \text{and} \quad 0.0 \leq \psi_{\text{fwd}} < \psi_{\text{aft}} \leq 1.0 \quad (67)$$

The average t/c (thickness-to-chord ratio, in percent) of a base composite-element airfoil i between the forward station ψ_{fwd} and the aft station ψ_{aft} is

$$t/c \text{ elem}_i = \frac{\int_{\psi_{\text{fwd}}}^{\psi_{\text{aft}}} 2\zeta_i(\psi) d\psi}{\psi_{\text{aft}} - \psi_{\text{fwd}}} \quad (68)$$

Let $\tau_{ave,ij}$ be defined as the local average t/c value for composite wing ij at the constraint spanwise station η_{con} :

$$\tau_{ave,ij}(\eta_{\text{con}}) = t/c \text{ elem}_i \cdot Sy_j(\eta_{\text{con}}) \quad (69)$$

This can be converted into a vector relation using the transformation process described by Eqs. (18) and (19). This results in

$$\tau v_k \equiv \tau_{ave,ik,jk_k} \quad (70)$$

The individual composite average thickness constraints for each of the composite wings vary directly with the scaling factors s_i . The total thickness constraint equation is then

$$\tau_{\text{des}} = \sum_k s_k \tau v_k \quad (71)$$

where τ_{des} is the desired average t/c over the chordwise interval $\Delta\psi = \psi_{\text{aft}} - \psi_{\text{fwd}}$ at spanwise station η_{con} .

$$\begin{bmatrix} 2D_{11} & D_{12} & D_{13} & - & - & D_{1N} & 1 & \tau c n_1 \\ D_{21} & 2D_{22} & D_{23} & - & - & D_{2N} & 1 & \tau c n_2 \\ D_{31} & D_{32} & 2D_{33} & - & - & D_{3N} & 1 & \tau c n_3 \\ - & - & - & - & - & - & - & - \\ - & - & - & - & - & - & - & - \\ D_{N1} & D_{N2} & D_{N3} & - & - & 2D_{NN} & 1 & \tau c n_N \\ 1 & 1 & 1 & 1 & 1 & 1 & 0 & 0 \\ \tau c n_1 & \tau c n_2 & \tau c n_3 & - & - & \tau c n_N & 0 & 0 \end{bmatrix} \begin{bmatrix} k_1 \\ k_2 \\ k_3 \\ - \\ - \\ k_N \\ \lambda_v \\ \lambda_r \end{bmatrix} = \begin{bmatrix} -Dwb_1 \\ -Dwb_2 \\ -Dwb_3 \\ - \\ - \\ -Dwb_N \\ VR \\ \tau des \end{bmatrix}$$

Fig. 14 System of equations for optimization with a local thickness constraint.

Normalize this equation by the volume ratio of each of the composite wings to obtain

$$\tau des = \sum_k (s_k v_k) \frac{t v_k}{v_k} \quad (72)$$

Define

$$\tau c n_k \equiv \frac{t v_k}{v_k}$$

The average thickness constraint equation becomes

$$\phi T = \tau des - \sum_{q=0}^{Nt-1} k_q \tau c n_q = 0 \quad (73)$$

Following the same procedure as before, we obtain the linear set of equations for determination of the shape of the wing for minimum wave drag in the presence of the body and with both a wing volume constraint and a local average t/c constraint, as shown in Fig. 14.

Each local thickness constraint adds an additional row and column to the D matrix and an additional row to the k and R matrices. The optimum solution is once again obtained as a simple matrix inversion as

$$[k] = [D][R]^{-1}$$

X. Initial Validation of the FCE Optimization Process

During the early U.S. SST program (circa 1961), Boeing conducted a supersonic wing optimization study using an early version of an aerodynamic influence coefficient (AIC) panel method. The objective of the study was to determine the optimum wing spanwise thickness distribution for a delta wing configuration at supersonic speeds. The optimized process was formulated to maximize wing volume for a constant wave drag at the design Mach number of 3.0. The airfoil shape was held constant across the wing span. The thickness/chord ratio for the initial reference wing for the study was constant across the wing span and equal to 2.4%. The study configuration is shown in Fig. 15.

The optimized configuration and the reference constant- t/c configurations were built and tested in the Boeing supersonic wind tunnel and the Boeing transonic wind tunnel. The design Mach number was 3.0.

Figure 16 contains the experimental wave-drag measurements for both the baseline and optimized configurations. The experimental wave drag was obtained by subtracting calculated fully turbulent flat-plate skin-friction drag from the test data. The figure also contains recent far-field wave-drag predictions for each configuration. The optimized configuration, as shown in the figure, had an 18.8% increase in wing volume relative to the baseline constant- t/c wing/body configuration.

Above Mach 2.0, the wings had supersonic leading edges for which the Mach number normal to the leading edge was equal to, or greater than, Mach 1.0. Above Mach 2.0, the theory and test data indicate that both models had the same wave drag even though the volume of the optimized wing was substantially larger than the baseline-wing configuration.

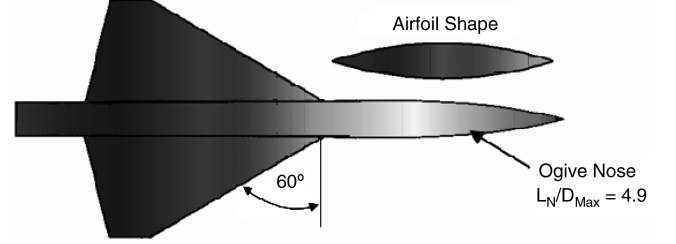


Fig. 15 Design optimization test case configuration.

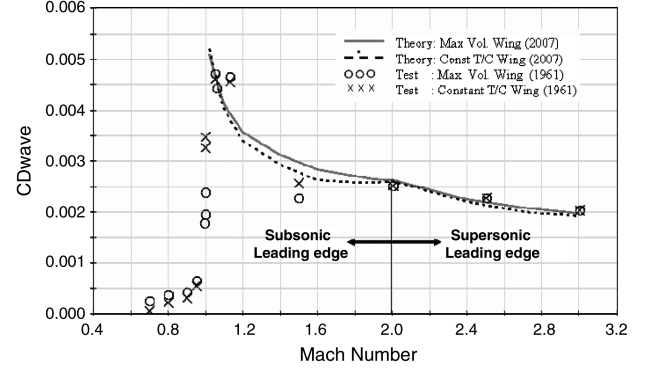


Fig. 16 Comparison of theoretical and experimental wing/body wave drag.

The solution process for minimum wave drag for a given volume is identical to the solution process for maximum volume for a given wave drag. The only difference is a constant scaling of the wing thickness. For the present study, it was decided to optimize the spanwise thickness distribution for a fixed wing volume. The 1961 AIC optimum wing thickness was then reduced to be equal to the volume of the reference 2.4% constant- t/c wing, and the wave drag for the scaled optimum wing was calculated.

For the FCE optimization study, the wing geometry was described by a series of composite-wing shapes corresponding to the biconvex airfoil. The equation for a biconvex airfoil is

$$\zeta(\psi) = Sx \cdot C_{1,0}^{1,0}(\psi)$$

where $Sx = 2(t \max / c)$.

The spanwise thickness variation was represented by various orders of Bernstein polynomials (BPOs). The total analytic surface was therefore described by the equation

$$\zeta(\psi, \eta) = \sum_{j=0}^{Ny-1} s_j C_{1,0}^{1,0}(\psi) \cdot Sy_j(\eta) \quad (74)$$

where s_j are the to-be-determined optimum scaling factors, and Ny corresponds to the selected order of the spanwise BPO, which was varied from 0 to 6 in the present study to explore convergence of the optimized optimum solution with increasing numbers of composite-wing elements. Figure 17 shows the composite-wing elements corresponding to a spanwise BPO = 3 representation.

Results of the optimization study are shown in Fig. 18 for the range of studied composite-wing sets corresponding to the various BPO designs. The results shown in the figure include constant-volume isolated-wing optimized designs with and without outboard t/c constraints. The t/c constraints restricted the outboard-wing thickness/chord to a minimum of 2%. The results indicate that the optimum solutions rapidly converged for BPO of 2 and above.

Figure 19 shows comparisons of the FCE BPO = 3 optimized design with 4 variables with the 1961 AIC optimization results that used 10 design variables. The results of the current and previous studies are essentially identical.

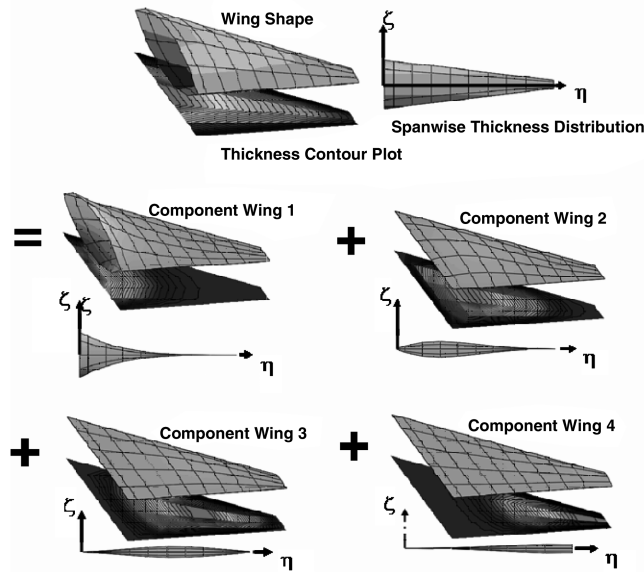


Fig. 17 Composite-wing shapes for spanwise bernstein polynomial of order 3.

Figure 20 shows the far-field analyses' wave-drag distributions for the optimized designs as a function of the cutting-plane angle. The $\theta = 0$ deg value corresponds to the momentum drag loss in the plane of the wing. For a vertically symmetric configuration, the $\theta = 90$ deg drag value is equal to that at $\theta = -90$ deg, which corresponds to the momentum loss below the airplane. This is the value most often used to calculate sonic boom. Equivalent area plots are also shown for three different cutting-plane angles.

The theoretical lower-bound wave drag is also shown in the figure. This corresponds to every equivalent body shape for all θ angles with the same area distribution as an equivalent-volume and equivalent-length Sears–Haack body. For most planforms, this is an impossibility. However, the lower-bound drag is often used to serve as a measure of the goodness of a wing design.

XI. Combined Wing Airfoil Shape and Thickness Distribution Optimization

The FCE optimization method and the CST analytic wing representation technique were used to conduct a design optimization study to minimize the wave drag of the arrow-wing and ogive/cylinder configuration shown in Fig. 21.

The wing planform was defined by four parameters: wing area, aspect ratio ($AR = 1.65$), taper ratio (0.1), and leading-edge sweep ($\Lambda_{LE} = 71.2$ deg).

The body geometry was defined by a total of 5 design parameters: 1) overall body length, 2) body maximum diameter, 3) nose length, 4) aft body length, and 5) nose and aft body ogive-distribution class function, $ND1 = ND2 = 1.0$.

The overall wing airfoil class-function exponents were $N1 = 0.5$ and $N2 = 1.0$, corresponding to a fundamental round nose with the finite boat-tail-angle class of airfoils.

The analytic wing shape definition for the optimization studies included representation of the basic airfoil shape by a set of four composite airfoils, corresponding to a BPO = 3 representation of the airfoil shape function. The spanwise variation of each of the composite airfoils was described by BPO = 2 representations. The composite airfoil shapes and spanwise variation components are shown in Fig. 22. This resulted in a family of 12 composite-wing geometries corresponding to three spanwise thickness variations for each composite airfoil. The 12 scaling coefficients for the composite-wing geometries were the design optimization variables.

The analytic wing definition of the arrow-wing shape is therefore

$$\zeta(\psi, \eta) = \sum_{j=0}^2 S y_j(\eta) \sum_{i=0}^3 s_{ij} C_{1,0}^{0.5}(\psi) S x_i(\psi) \quad (75)$$

The optimization studies were conducted for two supersonic Mach numbers: Mach = 2.4 and 3.3.

At Mach 2.4, the wing has a subsonic leading edge because the freestream Mach lines are swept less than the wing leading edge. The wing leading-edge normal Mach number for this case is equal to 0.773.

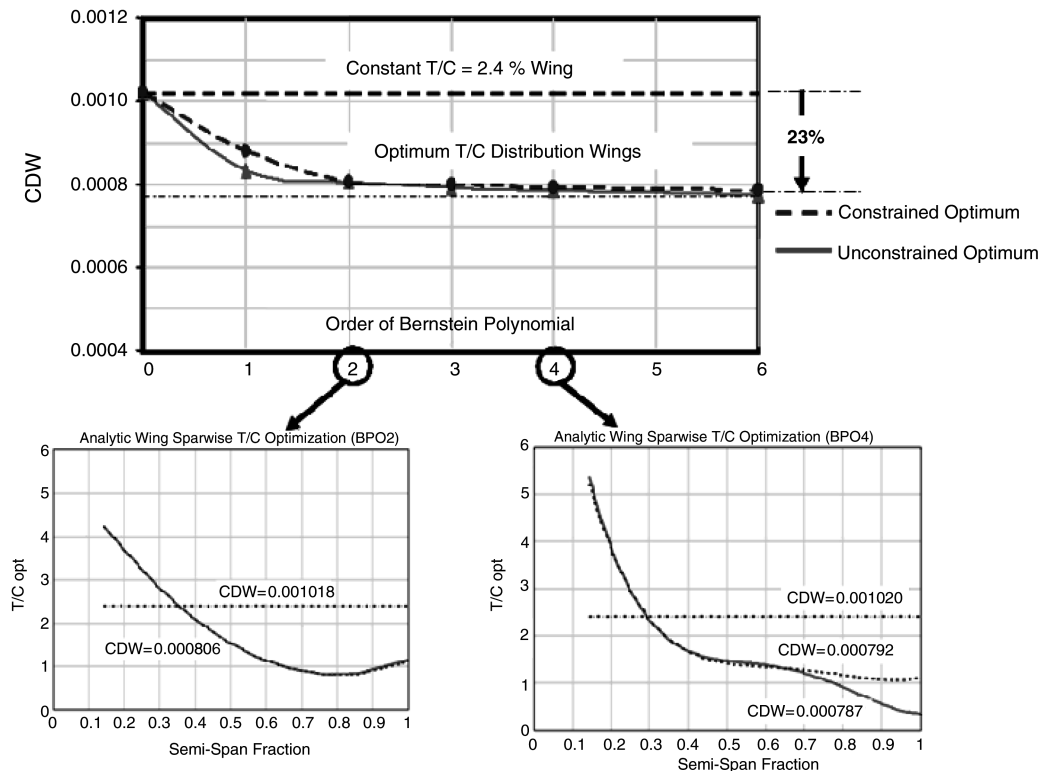


Fig. 18 Effect of spanwise BPO variation on optimized wave drag.

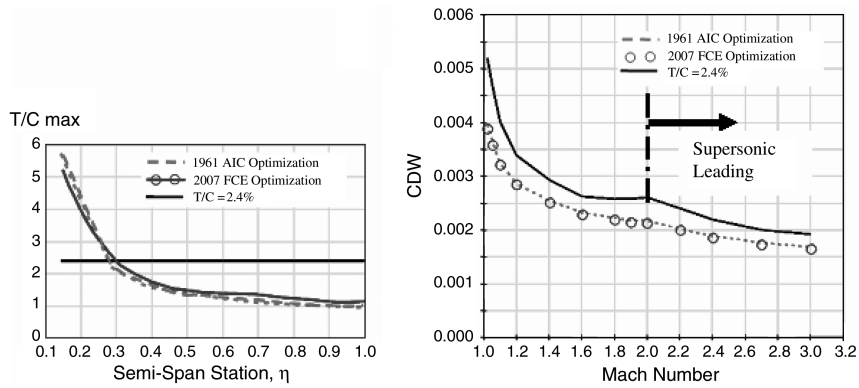


Fig. 19 Comparisons of FCE and AIC wing optimization results.

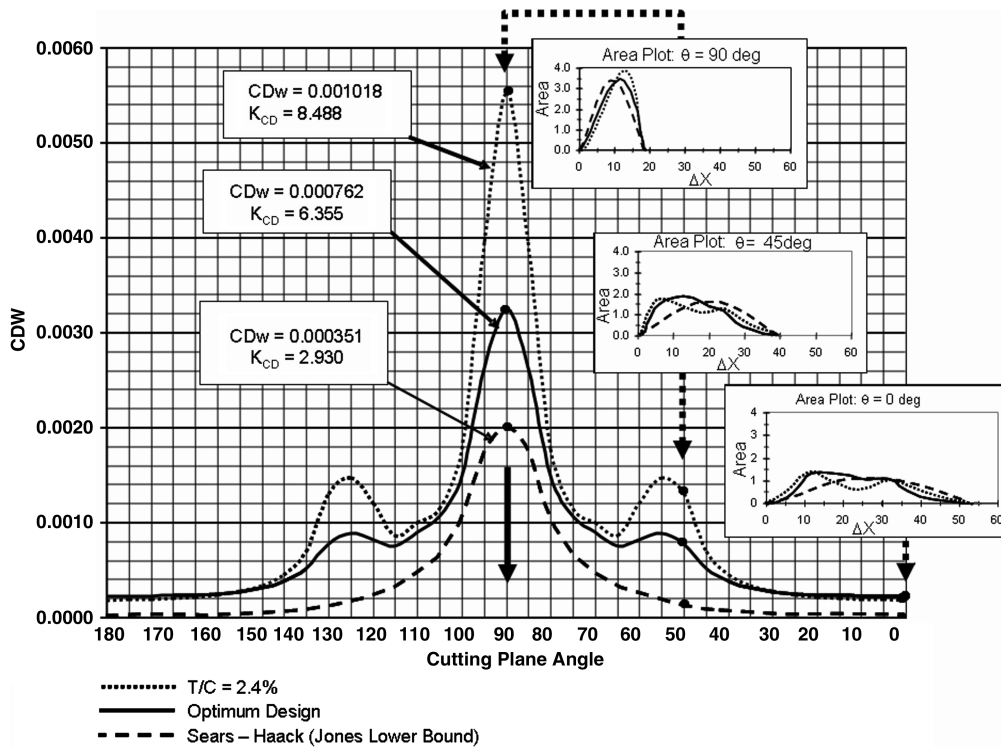


Fig. 20 Comparisons of isolated-wing far-field wave-drag distributions.

At Mach 3.3, the wing has a supersonic leading edge because the freestream Mach lines are swept more than the wing leading edge. The wing leading-edge normal Mach number for this case is equal to 1.064.

The optimization studies included four cases: Case 1 is isolated-wing optimization. Case 2 is isolated-wing optimization in the presence of the ogive/cylinder (O/C) body. Case 3 is isolated-wing

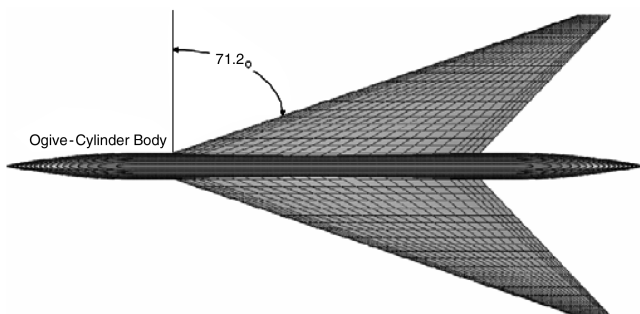
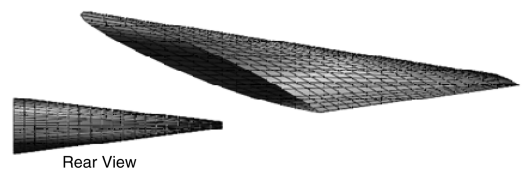


Fig. 21 Arrow-wing/body study configuration.

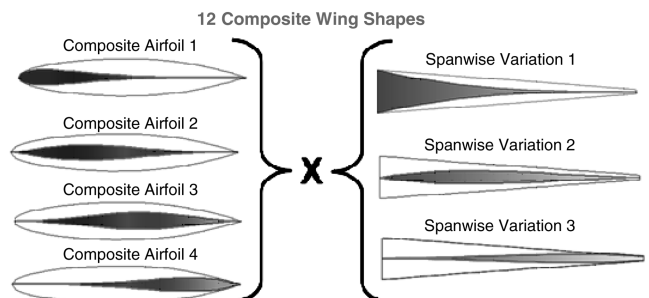


Fig. 22 Baseline-wing analytic representation of composite elements.

optimization with an outboard thickness. Case 4 is isolated-wing optimization with an outboard thickness in the presence of the body.

The reference wing for the drag comparisons was an equal-volume wing with a constant-thickness/chord-ratio t/c biconvex airfoil. The t/c was equal to 3.45%.

XII. Mach 2.4 Subsonic Leading-Edge Wing Optimization Results

The results for the design Mach number of 2.4 will be initially discussed. Figure 23 shows the results for of the isolated-wing optimization, case 1. The wave drag for the optimum isolated-wing is seen to be 29.3% less than the reference configuration. When analyzed with the body, the isolated optimum wing is about 23.4% less than the reference wing/body. Wing section airfoils across the span are compared with the reference-wing airfoil sections. Relative to the reference-wing geometry, the optimum airfoil sections have rounded leading edges, and the location of the maximum thickness appears to move from aft on the inboard wing to more forward on the outboard wing. The wing trailing-edge closure angle for most of the outboard portion of the wing is less than that of the reference wing. These differences will be discussed in greater detail further along in the paper.

The optimum isolated-wing thickness distribution becomes rather thin near the wing tip. Consequently, a wing thickness constraint was added at 95.2% of the wing span to ensure that the wing thickness would never be less than 2% across the wing, and the isolated-wing was reoptimized with the thickness constraint. Results of the

isolated-wing optimization obtained with the outboard t/c constraint are shown in Fig. 24. Restricting the wing to be no less than 2% thick had an extremely small effect on the wave drag of the optimum wing and on the optimum wing/body.

The results of optimizing the wing in the presence of the body are shown in Fig. 25. The isolated-wing drag with the thickness constraint is only very slightly higher than the optimum isolated wing; however, the combined wing/body drag is slightly lower (23.6% lower) than the reference wing/body relative to 23.4% reduction achieved for the case of the isolated optimum wing. In this case, the presence of the favorable body interference on the wing resulted in an increase in the local wing thickness on the outboard wing near the tip and also at the side of the body. Consequently, it was not necessary to include an outboard-wing thickness constraint when the body effects were included.

Figures 26–29 contain detailed comparisons of the characteristics of the previously discussed optimized wing designs with the corresponding parameters for the reference wing. The spanwise variations of the maximum thickness/chord are shown in Fig. 26. The optimum isolated-wing t_{max}/c decreases continually over the entire wing span. This indicates that the nominal drag per unit area is relatively high near the wing tip. The single outboard-wing thickness constraint resulted in a maximum thickness distribution that was greater than 2% over the entire wing span.

The optimization of the wing in the presence of the body had a rather significant effect on the wing maximum thickness distribution. For this case, the spanwise distribution of the maximum thickness over the entire wing was greater than 2%. Hence, no thickness

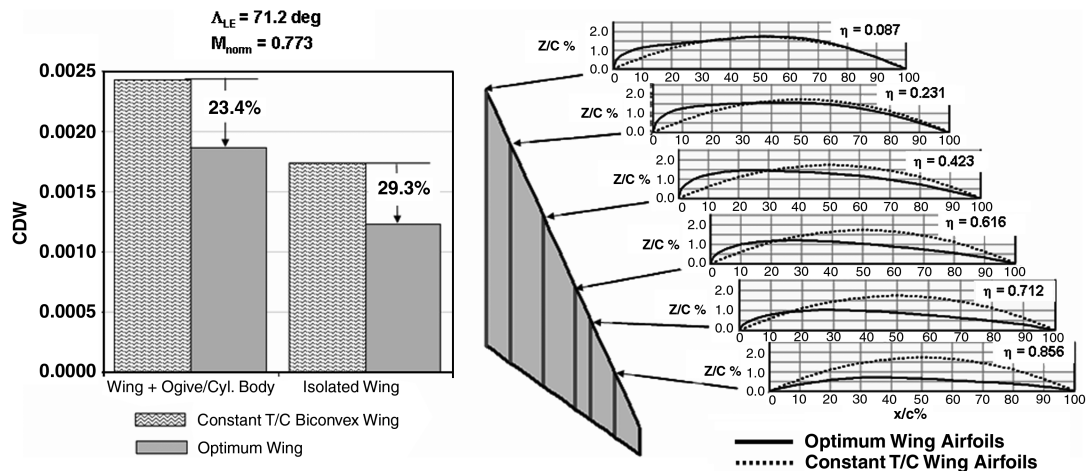


Fig. 23 Mach 2.4 optimum isolated-wing design with a constant wing volume.

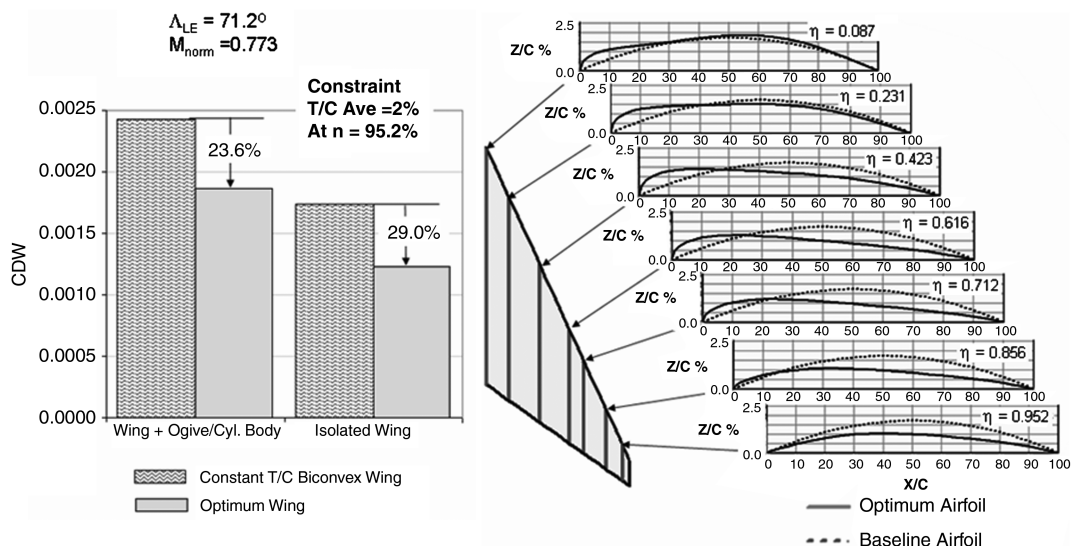


Fig. 24 Mach 2.4 optimum isolated-wing design with constant wing volume and outboard depth constraint.

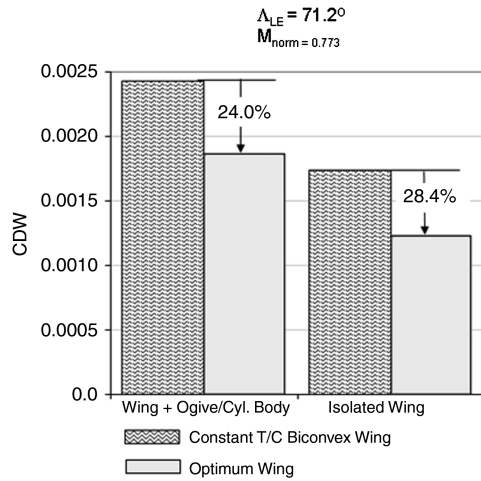


Fig. 25 Mach 2.4 optimum wing in the presence of the ogive/cylinder body.

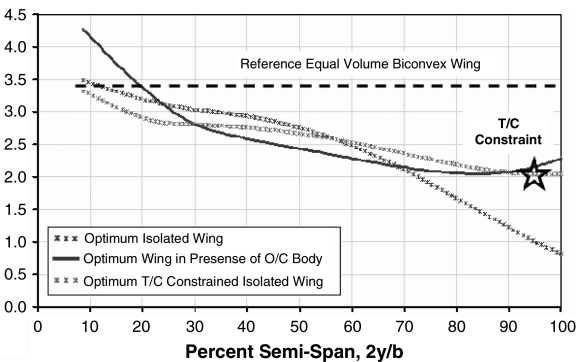
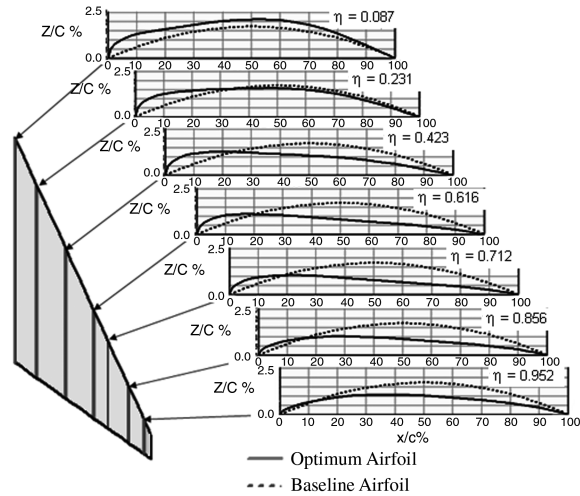


Fig. 26 Mach 2.4 optimum t_{max}/c spanwise distribution.

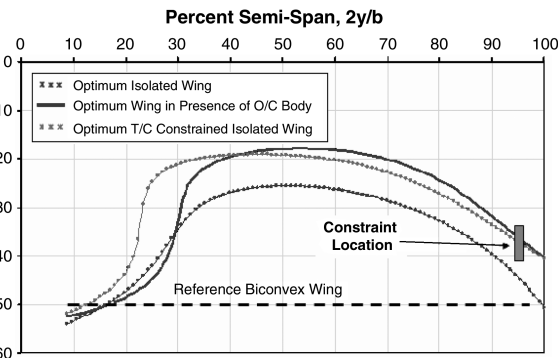


Fig. 27 Mach 2.4 optimum t_{max}/c spanwise location.

constraint was required. Relative to the isolated optimum wing, the wing thickness near the inboard region was increased as well as in the outboard region. The midspan thickness distribution was decreased. Areas of increased thickness on the wing thickness tend to imply that the body interference effects are favorable in those regions. Conversely, reduction in wing thickness tends to indicate that in those regions the body interference is unfavorable.

The chordwise locations at which the maximum thickness occurs are shown in Fig. 28. The location of the maximum thickness is aft near midchord by the side of the body station and rapidly moves forward and remains forward over most of the midspan regions of the wing and then moves aft over the outboard region of the wing. The outboard-wing constraint as well as the body resulted in approximately 6 to 8% further forward movement of the maximum thickness location.

The spanwise distributions of the leading-edge-radius/wing-chord ratio R_{LE}/c for each of the optimized wing designs are shown in Fig. 28. The leading-edge radius depends not only on the airfoil

shape, but also on the airfoil thickness/chord ratio. In fact, the value of R_{LE}/c varies with $(t_{max}/c)^2$. Consequently, the parameter $(R_{LE}/c)/(t_{max}/c)^2$ can be considered as an indicator of the fundamental leading-edge bluntness of an airfoil. This bluntness parameter for each of the optimized wings is also shown in Fig. 28.

The study reference wing with a constant- t/c biconvex airfoil has a zero-radius pointed nose. Therefore, the leading-edge radius and bluntness parameter for an equal-volume wing with a constant 3% round-nose 65A-Bic airfoil is shown to give an indication of the relative bluntness of the optimized airfoil designs. The 65A-Bic airfoil shape has often been used in preliminary design supersonic transport studies.

All of the optimized wing designs have much greater bluntness than a 65A-Bic airfoil. The outboard-wing thickness constraint as well as the presence of the body substantially increased the bluntness of the wing over the entire wing outboard of 20% semispan.

The spanwise distributions of the trailing-edge closure angles for the optimized wing designs are shown in Fig. 29. The closure angle depends on both the fundamental shape of an airfoil as well as its maximum thickness/chord ratio. Consequently, the ratio of the closure angle to t_{max}/c provides a fundamental measure of the bluntness of the trailing edge of an airfoil. The comparisons in Fig. 29 indicate that the optimum thickness wings have substantially reduced closure angles over most of the wing. This reduction is primarily due to increased trailing-edge sharpness of the optimized designs. This indicates that a substantial amount of the drag reduction through optimization is most likely due to a decrease in the strength of the trailing-edge shock system.

Further insight into the nature of the optimized wing designs can be gained from inspection of the wave-drag distribution as a function of the cutting angle, as shown in Fig. 30.

A large source of the wave drag of the reference constant- t/c biconvex wing occurs when the cutting-plane angle is very close to the sweep of the trailing edge. This is associated with the trailing-edge recovery shock. As previously discussed, the optimum wing designs had reduced trailing bluntness, which indeed did decrease the wave drag in the region of the trailing-edge cutting plane.

It is interesting to note the increased drag of the optimum wings near the $\theta 90$ deg cut. The area distribution associated with this cutting plane is used to calculate the strength of the sonic boom below the airplane flight path. The increased wave drag implies that the optimum wing designs would conceivably increase the strength of the sonic boom.

XIII. Mach 3.3 Supersonic Leading-Edge Wing Optimization Results

The results of the wing optimization conducted at a Mach number of 3.3 are shown in Figs. 31–33. In these studies, the wing was optimized both with and without the presence of the body, and also

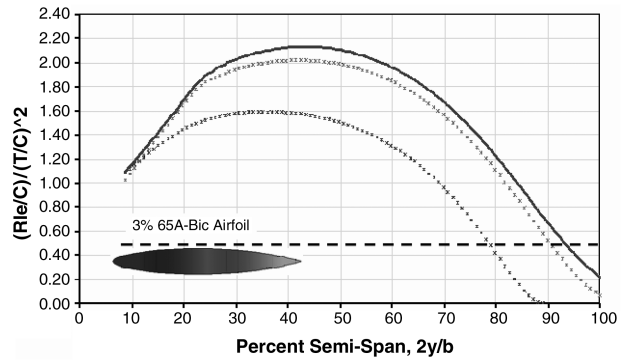
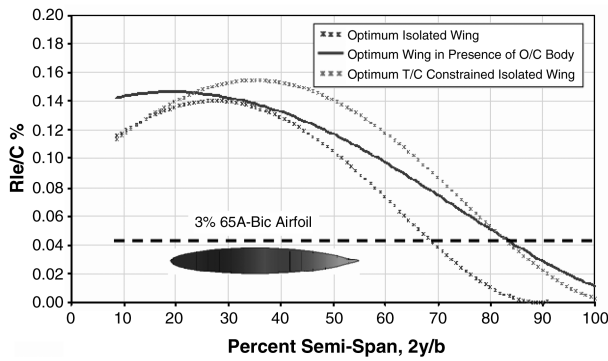


Fig. 28 Leading-edge radius and nose bluntness distribution.

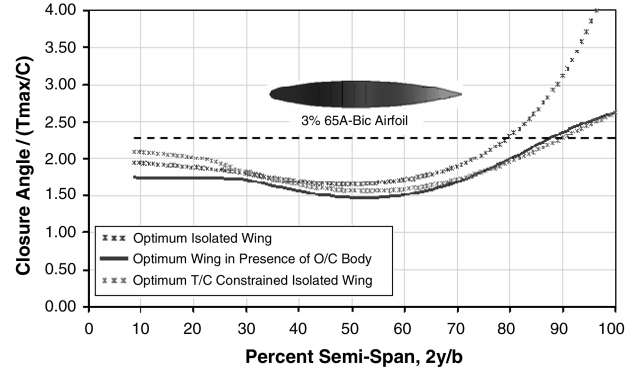
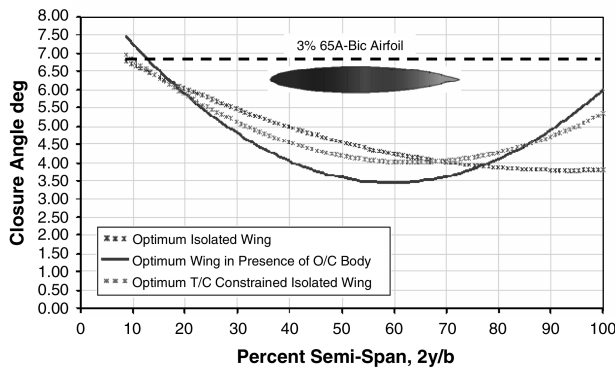


Fig. 29 Mach 2.4 optimum designs closure angle and trailing-edge bluntness distribution.

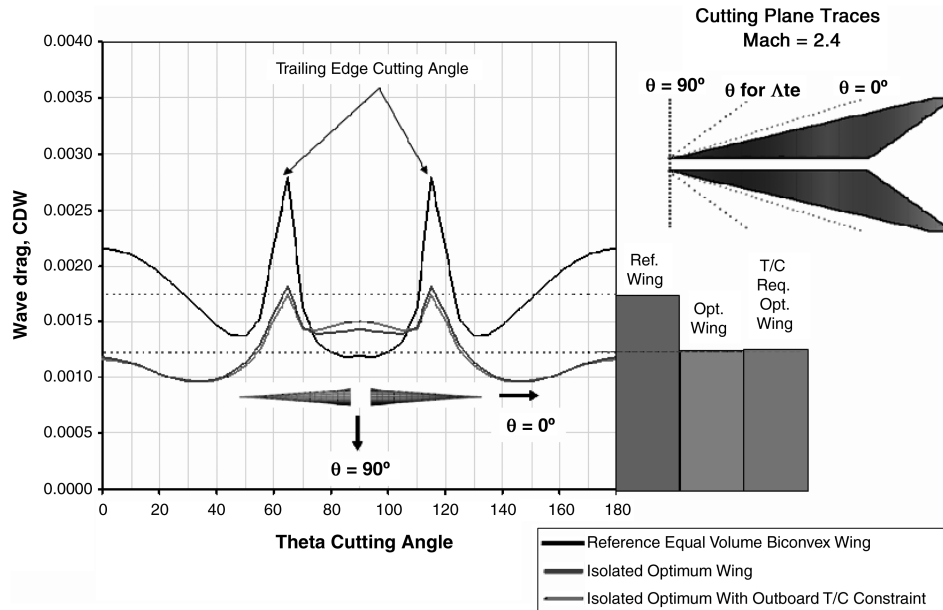


Fig. 30 Mach 2.4 optimum and reference isolated-wing wave-drag distributions.

with and without an outboard-wing t/c constraint. At the design Mach 3.3, the planform has a supersonic leading edge. The optimized spanwise distributions of t_{\max}/c are shown in Fig. 31. The chordwise locations at which the maximum thickness occurred are shown in Fig. 32.

The isolated optimized wing and the wing optimized in the presence of the body resulted in thickness distributions for which the maximum thickness was much less than 2% of the local chord over most of the outboard part of the wing. Consequently, a single thickness constraint was imposed at 71.1% of the wing semispan to ensure that t_{\max}/c would not be less than 2.0% on the wing. The optimum thickness distributions have similar characteristics, in

which t_{\max}/c is large near the wing root then decreases near midspan and then increases toward the wing tip. These thickness distributions are significantly different from the Mach 2.4 results (Fig. 26).

The chordwise location of the wings optimized without the t_{\max}/c constraint varied from midchord at the wing root and moved aft to about 70% of the wing chord at about three-fourths of the wing span and then moved forward to about 40% chord near the wing tip. The wing thickness constraint had a rather significant effect in the chordwise location of the maximum thickness by greatly restricting the chordwise movement of the maximum thickness location across the wing span.

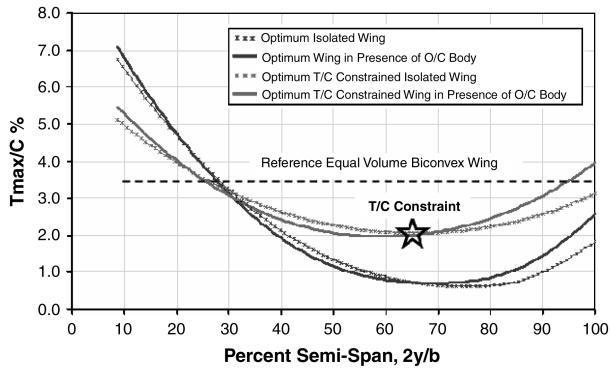


Fig. 31 Mach 3.3 optimum $t \max / c$ spanwise distribution.

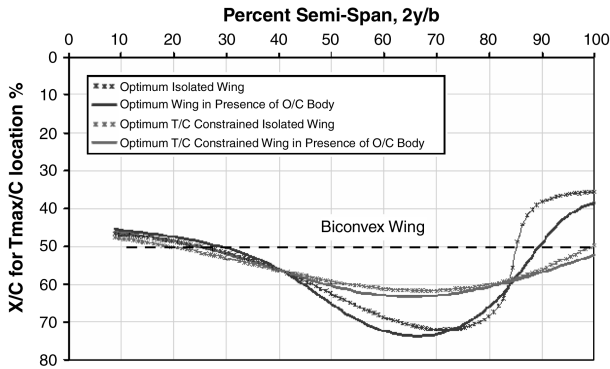


Fig. 32 Mach 3.3 optimum $t \max / c$ chordwise location.

Airfoil section shapes for the t/c constrained optimum isolated wing are shown in Fig. 33. The optimized airfoils have sharp leading edges, as would be expected for a supersonic leading-edge wing. The chordwise movement of the wing maximum thickness location is readily apparent. The leading edge of the optimum wing has significantly less nose angle relative to the baseline wing. This obviously results in a reduction of the wing leading-edge shock system.

These results illustrate the versatility for the CST parametric representation methodology. The composite-wing shapes used for both the Mach 2.4 and the Mach 3.3 optimization studies were

developed from the round-nose/sharp-trailing-edge class of airfoils with the class function $C_{1,0}^{0.5}(\psi) = \psi^{0.5}(1 - \psi)^{1.0}$.

A sharp-leading-edge/sharp-trailing-edge airfoil is fundamentally defined by the class function $C_{1,0}^{1.0}(\psi) = \psi(1 - \psi)$. However, as shown in this study, sharp-nose airfoils were adequately simulated by with a relatively few composite airfoils derived from the round-nose unit airfoil.

The wave drags for the optimized isolated wings and the wings optimized in the presence of the body are shown in Fig. 34. The optimized designs show significant reductions in zero-lift wave drag relative to the equal-wing-volume reference constant- t/c biconvex-wing configuration.

Figure 35 shows the distribution of the wave drag as a function of the cutting-plane angle. It is seen that a large source of the wave drag for the reference wing is associated with the leading-edge shock. This indeed was the source of the greatest drag reduction for the optimum wing designs. The t/c constrained optimum slightly increased the drag of the trailing-edge shock system.

The linear theory optimum airfoil shape for a given cross-sectional area is a biconvex airfoil that is symmetric about the midchord. The effect of sweep back for a wing with supersonic leading edges, as shown in Fig. 33, is to move the chordwise location of maximum thickness aft. According to the reverse-flow theorem [15], the drag of

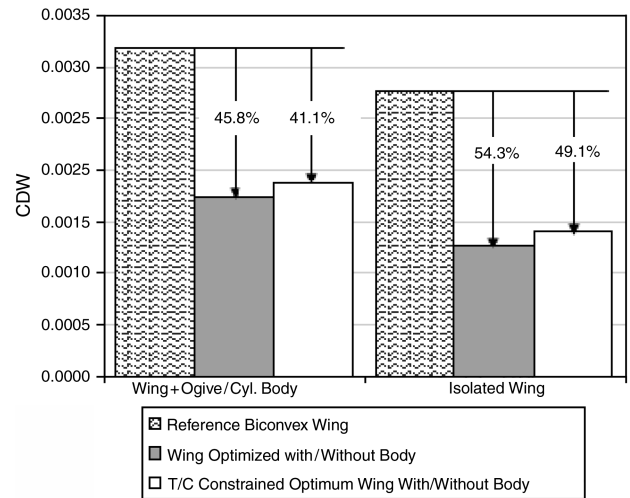


Fig. 34 Mach 3.3 wave-drag optimization results.

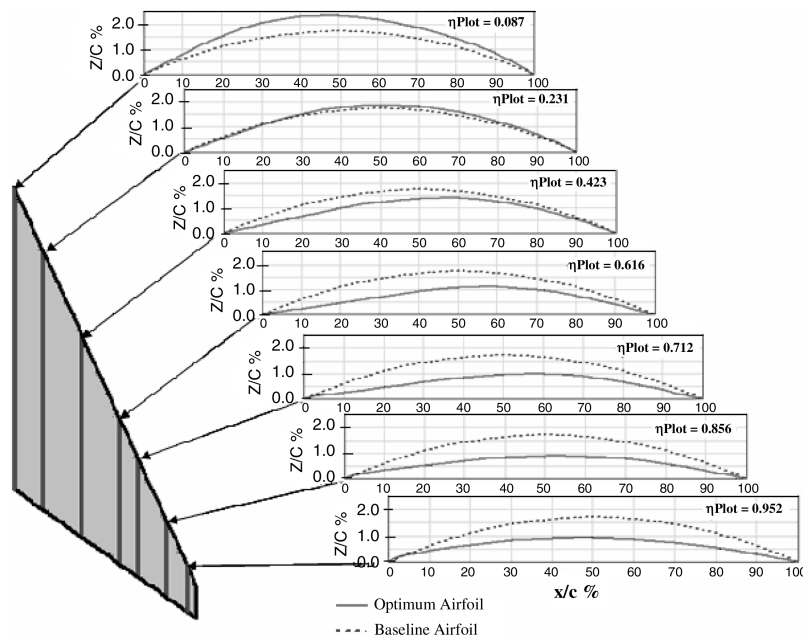


Fig. 33 Isolated optimum wing section shapes with t/c constrained.

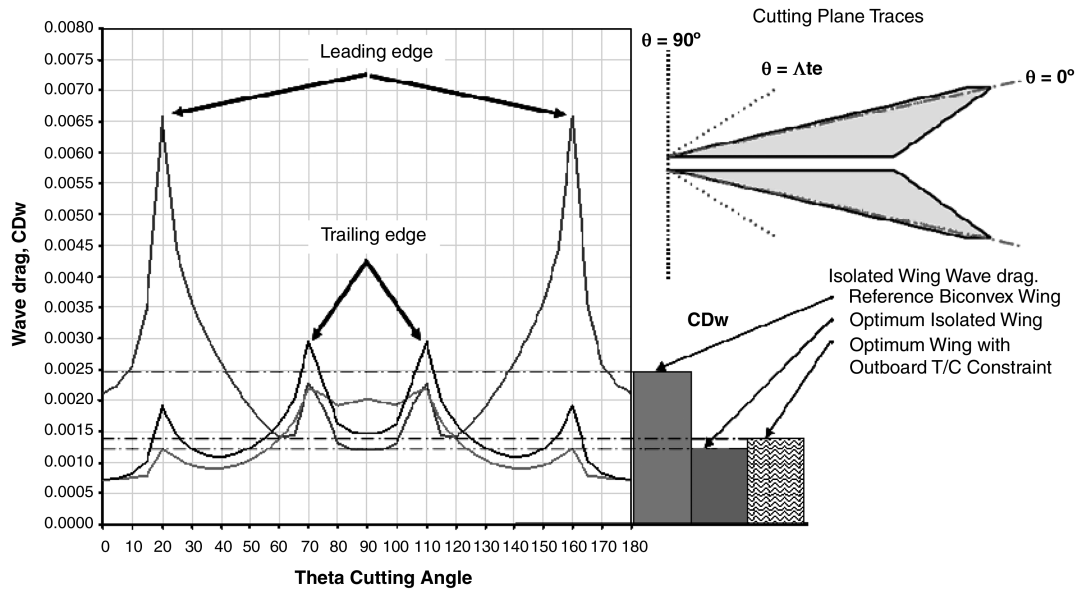


Fig. 35 Mach 3.3 optimum and reference isolated-wing wave-drag distributions.

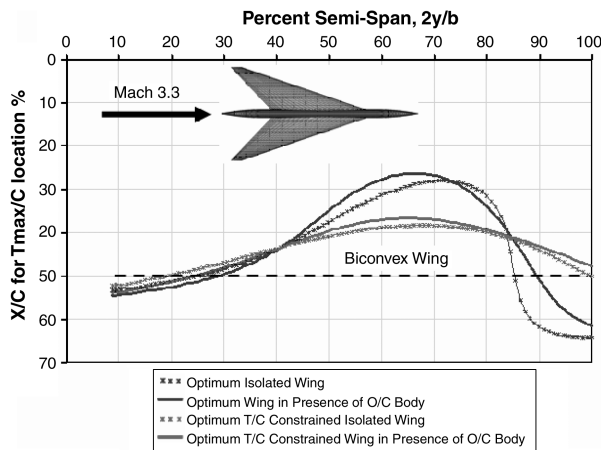


Fig. 36 Mach 3.3 swept-forward wing optimum T_{\max}/C chordwise location.

a given volume or thickness distribution is the same in forward and reverse flow. Therefore, the optimum solutions for the study's swept-back configuration are also the optimum solutions for the equivalent reverse-flow swept-forward configuration. The optimum wave drag and the optimum spanwise distribution of t_{\max}/c for the swept-forward configuration is the same as in Figs. 34 and 31, respectively. However, the chordwise location of the maximum thickness moves forward of the midspan location, as shown in Fig. 36.

XIV. Far-Field Wave Drag and FCE Paradox

The far-field wave-drag method is based on the fundamental assumption that the control volume for the drag calculation process is so far from the wing and body that the details of the configuration shape do not matter. However, the FCE optimization method that uses the far-field wave-drag method determines how to shape the wing, and so the geometry does matter.

XV. Conclusions

The good agreement between linear theory predictions of the cruise drag polars for supersonic transport configurations justifies the continued use of linear theory methods in the preliminary design development and trade studies, both individually and in conjunction with nonlinear CFD methods. A new method (FCE) for optimizing zero-lift wave drag of supersonic configurations using the CST universal parametric geometry method was presented. The FCE

methodology also allows easy and efficient exploration of the effects of various design constraints on minimum zero-lift wave drag. The integration of the FCE optimization with the new CST geometry representation technique was shown to provide a simple and an effective systematic and powerful design optimization process. The CST analytic representation methodology provides a very large design space of analytic wing representations with a relatively few number of design variables. The concept of the CST analytic wing definition was shown to be an effective geometric representation method for design optimization.

References

- [1] Kulfan, B. M., and Bussoletti, J. E., "Fundamental Parametric Geometry Representations for Aircraft Component Shapes," AIAA Paper 2006-6948, Sept. 2006.
- [2] Kulfan, B. M., "A Universal Parametric Geometry Representation Method—CST," AIAA Paper 2007-0062, Jan. 2007.
- [3] Kulfan, B. M., "Recent Extensions and Applications of the 'CST' Universal Parametric Geometry Representation Method," AIAA Paper 2007-7709, Sept. 2007.
- [4] Wilcox, D. C., *Turbulence Modeling for CFD*, DCW Industries, La Canada, CA, 2006, p. 3.
- [5] Kulfan, R. M., and Sigalla, A., "Real Flow Limitations in Supersonic Airplane Design," AIAA Paper 78-147, Jan. 1978.
- [6] Kulfan, B. M., "Reynolds Numbers Considerations for Supersonic Flight," AIAA Paper 2002-2839, June 2002.
- [7] Kulfan, B. M., "Assessment of CFD Predictions of Viscous Drag," AIAA Paper 2000-2391, June 2000.
- [8] Harris, R. V., Jr., "An Analysis and Correlation of Aircraft Wave Drag," NASA TMX 947, Oct. 1961.
- [9] Middleton, W. D., and Lundry, J. L., "A Computational System for Aerodynamic Design and Analysis of Supersonic Aircraft," NASA CR-2715, Mar. 1976.
- [10] Kulfan, B. M., "Fundamentals of Supersonic Wave Drag," *Reports of the Institute of Fluid Science, Tohoku University*, Vol. 20, 2008, pp. 11–70.
- [11] Lomax, H., and Heaslet, M. A., "A Special Method for Finding Body Distortions that Reduce the Wave Drag of Wing and Body Combinations at Supersonic Speeds," NACA RM A55B16, May 1955.
- [12] Lomax, H., and Heaslet, M. A., "Recent Developments in the Theory of Wing-Body Wave Drag," *Journal of the Aeronautical Sciences*, Vol. 23, No. 12, 1956, pp. 1061–1074.
- [13] Lomax, H., "The Wave Drag of Arbitrary Configurations in Linearized Flow as Determined by Areas and Forces in Oblique Planes," NACA RM A55A18, 1955.
- [14] Jones, R. T., "Theory of Wing-Body Drag at Supersonic Speeds," NACA RM-A53H18a, Sept. 1953.
- [15] Ashley, H., and Landahl, M., *Aerodynamics of Wings and Bodies*, Addison Wesley, Reading, MA, 1965, p. 196.